Alma Mater Studiorum · Università di Bologna

Dipartimento di Fisica e Astronomia
Corso di Laurea in Fisica del Sistema Terra

IMPROVING SATELLITE-BASED QUANTIFICATION OF EXTREME PRECIPITATION EVENTS WITH LONG RETURN PERIOD

Tesi di laurea magistrale

Relatore:
Ch.mo Prof.
Vincenzo Levizzani

Correlatore:
Dott. Francesco Marra

Presentata da:
Matteo Siena

Sessione III
Anno Accademico 2020-2021

Abstract

Extreme precipitation causes large damage and replenish freshwater storage in arid regions. Quantitative information on extremes with low yearly exceedance probability is crucial for risk and water resources management, design of hydraulic structures and early-warning systems. Rain gauges offer relatively long and homogeneous records, but don't sample uniformly the Earth's surface, leaving vast areas completely ungauged. Satellite observations could help overcoming this limit, but suffer from estimation errors, which may propagate to the estimated extreme quantiles.

In this work, rain gauge and satellite data for two different regions, Israel and a portion of south-eastern Austria, are used to derive extreme quantiles associated to low yearly exceedance probability using the novel "Simplified Metastatistical Extreme Value" framework. Differences between satellite and rain gauge estimates are analyzed using a specifically developed error model with the aim of understanding how the current approaches could be refined and improved.

The results show that satellite based estimates of extreme quantiles are in good agreement with the rain gauges over Austria, while a slight overestimation is detected over Israel. The developed error model allowed us to predict errors in the estimated quantiles based on errors in the parameters of the statistical model. Correlations between the first two moments of the events' distribution and the statistical model parameters provide the bases for including prior information on satellite estimation errors in the estimation of extreme quantiles.

Sommario

Le precipitazioni estreme causano ingenti danni e riempiono i depositi di acqua dolce nelle regioni aride. Informazioni quantitative su eventi estremi con basse probabilità di superamento annuali sono cruciali per la gestione delle risorse idriche, la progettazione delle opere idrauliche ed i sistemi di allerta. I pluviometri sono caratterizzati da serie storiche relativamente lunghe ed omogenee, ma essi non ricoprono uniformemente la superficie terrestre, lasciando scoperte aree molto vaste. Le osservazioni satellitari possono aiutarci a superare questo limite, ma sono affette da errori di stima, i quali possono propagarsi fino alla stima dei quantili estremi.

In questa tesi, dati pluviometrici e satellitari relativi a due differenti regioni, Israele ed una parte dell'Austria sud-orientale, sono stati utilizzati per poter derivare quantili estremi associati a basse probabilità di superamento annuali tramite l'utilizzo del "Simplified Metastatistical Extreme Value" framework. Le differenze tra le stime satellitari e pluviometriche sono state analizzate tramite l'utilizzo di un modello di stima degli errori appositamente formulato per comprendere come gli attuali approcci possano essere rifiniti e migliorati.

I risultati mostrano che le stime dei quantili estremi ottenute sulla base dei dati satellitari sono in buon accordo con quelle pluviometriche per quanto riguarda l'Austria, mentre per Israele è stata evidenziata una lieve sovrastima. Il modello di propagazione degli errori utilizzato ha permesso di prevedere in modo adeguato gli errori nei quantili stimati, sulla base degli errori nei parametri del modello statistico utilizzato. Le correlazioni tra i primi due momenti della distribuzione degli eventi di precipitazione ed i parametri del modello statistico hanno permesso di includere le informazioni preliminari sugli errori di stima dei parametri nella stima dei quantili estremi.

Contents

List of Figures

Listings

Chapter 1

Introduction

1.1 Extreme Precipitation

1.1.1 Significance of Extreme events

Extreme events could be defined as events whose magnitudes lie in the upper or lower parts of the distribution. In this work, extreme precipitation events related to long return periods were studied. They are events with low yearly exceedance probability [Chow et al., 1988]: for instance, events with 100 years return period, termed 100-year return levels, are events with intensity likely to be exceeded with a probability of 1% (1/100) in a given year, and are thus expected to be exceeded, on average, once in 100 years.

Extreme precipitation affects several social, ecological, economic and technical systems, by causing natural hazards such as floods and landslides, and by replenishing freshwater storage in arid regions. Monitoring and quantifying extreme precipitation quantiles is thus crucial for several fields and applications, such as hydraulic structures design and weather-related risk management [Katz et al., 2002]. In addition, extreme precipitation events are of main concern in the context of the global warming: in fact, in the last decades many studies showed that extreme events are rising in intensity and changing in frequency, as shown in figure 1.1 [Berg et al., 2013, Myhre et al., 2019; Fischer and Knutti, 2016]. In order to improve the estimation of the probability of occurrence of extreme precipitation, accurate observations and adequate methods are needed. In this study, rain gauge and satellite estimates of daily precipitation over diverse climatic settings are analyzed using a novel statistical approach, with the aim of deriving quantiles associated with long return periods, evaluating the accuracy of the satellite-based estimates, and address some of the current methodological gaps in the precipitation frequency analyses based on satellite data.

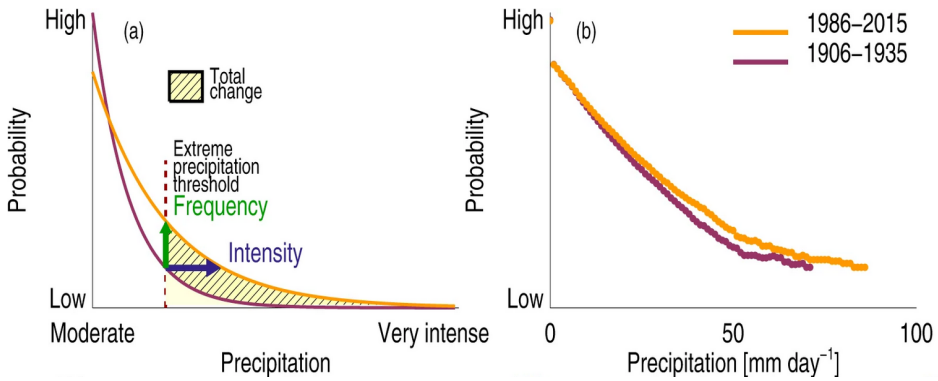

Figure 1.1: Probability Density Functions (PDF) for daily precipitation amounts. (a) The purple line is the reference PDF, the orange one shows how it changes with higher temperatures. (b) Changes in extreme precipitation between the periods 1906-1935 and 1986-2015 as a mean of actual observations of 15 rain gauge stations in the Netherlands [Myhre et al., 2019].

1.1.2 How to study extremes

Extreme return levels are usually quantified by means of the Extreme Value Theory, which studies the limiting distribution for extremes of large samples. From a practical standpoint, its formulations neglect a large portion of the observable events, because it focuses on the distribution of annual maximum values or of the peaks exceeding very large thresholds. This data decimation leads to large uncertainties in the estimated quantiles.

Additionally, Extreme Value Theory is sometimes limited by the underlying assumption on the asymptotic behaviour of the samples of the probability distribution function: an infinite number of events should occur every year. It was observed that the number of yearly observations (for example, the number of yearly wet days) is often too scarce for this asymptotic assumption to hold [Nerantzaki and Papalexiou, 2022].

New non-asymptotic statistical approaches were developed in the last years, such as the Metastatistical Extreme Value framework (MEV) [Marani and Ignaccolo, 2015; Zorzetto et al., 2016], which also allows to consider all the available samples to infer the distribution of extremes. Successively, a simplified formulation of MEV, termed Simplified Metastatistical Extreme Value framework (SMEV), was proposed as a way to better fit the statistical model to the observed extremes.

By exploiting these new approaches, quantiles related to extreme precipitation events can be derived from the distribution of the so-called ordinary precipitation events (see section 1.1.3 for a definition), with a considerable in-

crease of the data sample to be used for parameters and quantiles estimation and, consequently, of estimation accuracy.

1.1.3 Ordinary and extreme events

Ordinary precipitation events, which are the fundamental samples for frequency analyses studies, are defined as all the independent realizations of a process of interest [Marani and Ignaccolo, 2015; Marra et al., 2020].

For the case of precipitation, they can be considered as non-zero rainfall amounts observed in statistically independent rainy periods. In this work, since daily rain is analyzed, ordinary events are defined as stochastic realizations of independent daily rain amounts exceeding a predefined low threshold [Zorzetto et al., 2016].

As discussed above, extremes are very high samples of the ordinary events. The distribution of the ordinary events is typically unknown, but it is possible to approximate the tail of this distribution, i.e. the portion of the distribution which describes the probability of very high events, using relatively simple formulations. Practically, the tail of the ordinary events distribution can be identified by the portion of data which shares the statistical properties with the annual maxima.

For example, it was shown that for the case of daily precipitation, the exceedance probability of heavy intensities likely decreases as a stretched exponential, and can thus be described using a Weibull distribution [Wilson and Tuomi, 2005]. In estimating extreme return levels, it is thus good practice to focus on the tail of the distribution of ordinary events [Marra et al., 2020]. This tail can be detected using statistical tests which verify which portion of the distribution is likely sampled from a Weibull model: in fact, in previous studies, the Weibull distribution was used to describe ordinary events, but it was shown that it fits better to the tails [Marani and Ignaccolo, 2015; Miniussi and Marani, 2020; Zorzetto et al., 2016; Papalexiou, 2018].

1.2 The need for satellite observations

The earth surface is covered by rain gauges in an uneven way: for instance, ocean surface is characterized by very few data collected by buoys and ships; moreover, several parts of mainland are covered by an elevated number of stations (urban areas), while others present a very scarce coverage (arid areas and rainforests, for example).

In figure 1.2, the spatial distribution of the Global Precipitation Climatology Centre (GPCC) rain gauges, a global network characterized by regular

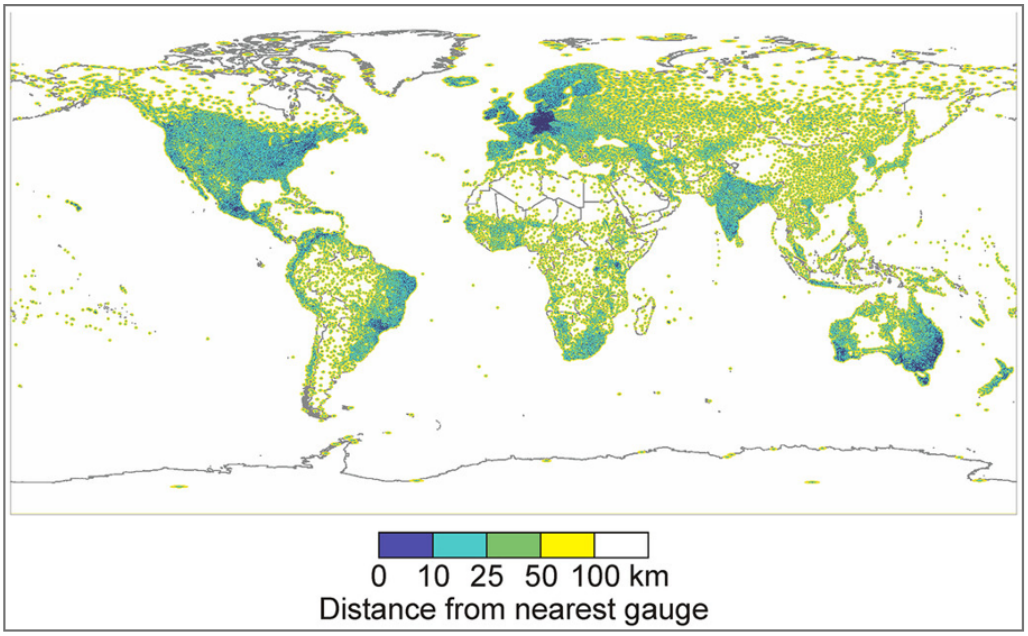

Figure 1.2: Spatial distribution of GPCC gauges [Kidd et al., 2017].

and reliable daily measurements [Becker et al., 2013], is shown. Assuming an average instrument orifice of 246 cm^2, the overall land coverage would be roughly of 1,612 m^2. A typical soccer pitch of 105 m x 68 m is characterized by an area of 7140 m^2, thus all GPCC stations in the world would not even cover one fourth of a pitch of such type [Kidd et al., 2017].

Satellite precipitation products have been characterized by a fast development in the last decades. They can provide information with quasi-global coverage (see figure 1.3) at a maximum resolution of roughly 4 km in space and 30 minutes in time [Michaelides et al., 2009]. These aspects make them more likely to be preferred with respect to rain gauges networks, since they can overcome their sampling limitations by observing vast regions and covering ungauged areas of the globe.

Despite the shortness of their records, which are currently in the order of 20-30 years at most, they started to be used for deriving high quantiles of interest for several applications [e.g., Gado et al., 2017]. Estimation errors, however, were found to severely affect the results [Marra et al., 2019a]. Precipitation frequency analysis methods based on satellite records are currently characterized by several gaps [Marra et al., 2019a], especially in case of satellite data evaluation and extrapolation [Hu et al., 2018]. In fact, even though they are used for quantile derivation, they show several estimation errors [Kidd and Levizzani, 2011] due to the indirect measurements, which

are enhanced for extremes [Miao et al., 2015; Prakash et al., 2015]. Furthermore, the currently adopted statistical methods for satellite records' analysis have proved to be inadequate due to the poor availability of data points to estimate the parameters of extreme value distributions [Marra et al., 2019a].

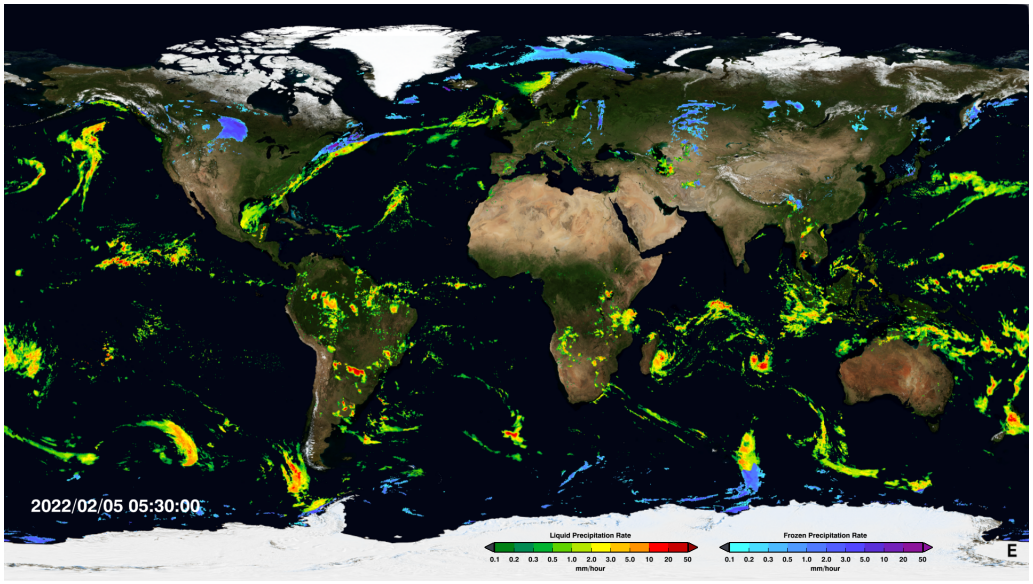

Figure 1.3: Typical half-hourly precipitation map from the Integrated Multi-satellitE Retrievals for GPM (IMERG) algorithm [NASA].

1.3 Specific objectives

This thesis directly addresses these gaps, with the aim of improving satellite based derivation of high return period quantiles. The following specific research questions have been addressed:

- How well do satellite products reproduce long return period quantiles over different climatic conditions using a novel statistical approach?
- Which portion of the ordinary events distribution shares the statistical properties of extremes?
- Which are the agreements and differences between land and satellite based instruments in deriving high return period quantiles and how well can these differences be predicted based on the satellite estimation errors?

- Are there correlations between parameters describing extreme return levels, which are derived quantities, and the moments of the distribution, which can be computed by prior knowledge of the ordinary events?

1.4 Thesis structure

In chapter 2 the theoretical structure of the applied SMEV statistical framework is described, right after having defined the MEV approach and discussed the differences with the classical EVT theory. Chapter 3 presents the analyzed data, both for land and satellite based ones. The applied methods for data analysis, parameters and quantiles estimation, error propagation and moments-parameters correlation are reported in chapter 4. The achieved results are described in chapter 5.

A final summary, reporting the thesis' findings and conclusions, can be found in chapter 6, along with an insight on future applications.

Chapter 2

Theoretical framework

2.1 Extreme Value Theory

Extreme Value Theory (EVT) [Gumbel, 1958] is a branch of statistics which focuses on very large (or small) events. It relies on the extreme value theorem [Fischer and Tippet, 1928; Gnedenko, 1943], which is analogous to the central limit theorem, but considers the distribution of maximum or minimum values instead of mean values.

Let's consider records of independent and identically distributed variables $X_1, X_2, ...$ (precipitation events under specific assumption, for instance), represented by the same cumulative distribution function F. If the samples are divided in "blocks", each consisting of n non-zero elements (annual records, for instance), then, the maximum of a specified block M_n (which would be an annual maximum) is defined by

$$M_n = max(X_1, ..., X_n) \tag{2.1}$$

Under these assumptions, the cumulative probability distribution of the block maxima, that is the probability of getting a value M_n not exceeding a threshold z, can be expressed as

$$\begin{aligned} Pr(M_n \leq z) &= Pr(X_1 \leq z, ..., X_n \leq z) \\ &= Pr(X_1 \leq z)....Pr(X_n \leq z) = F(z)^n \end{aligned} \tag{2.2}$$

A linear renormalization of the variable M_n is needed, since, if z_+ is the smallest value for which $F(z) = 1$, then, for any $z < z_+$, $F(z)^n \to 0$ for $n \to \infty$; i.e. the distribution degenerates into a single point on z_+. If a_n and b_n are sequences of constants, such that $a_n > 0$, then the normalization can be achieved as follows:

$$M_n^* = \frac{M_n - b_n}{a_n} \tag{2.3}$$

Now, the focus is on seeking limit distributions for M_n^* by appropriately choosing a_n and b_n in order to stabilize the distribution parameters (location, scale) of M_n as n increases. From these results, it can be proved that, if there exist sequences of constants a_n and b_n, with $a_n > 0$, such that

$$\lim_{n\to\infty} P\left\{M_n^* \leq z\right\} = G(z) \tag{2.4}$$

or

$$\lim_{n\to\infty} F(a_n z + b_n)^n = G(z) \tag{2.5}$$

and if $G(z)$ is a non degenerate distribution function, then G(z) belongs to one of three main families of distributions [Fischer and Tippett, 1928]:

- Gumbel (Type I)

$$G(z) = e^{-e^{-\frac{z-b}{a}}} \quad \text{with} \quad -\infty < z < +\infty \tag{2.6}$$

- Frechet (Type II)

$$G(z) = \begin{cases} 0, & \text{if } z \leq b \\ e^{-\frac{z-b}{a}^{-\alpha}}, & \text{if } z > b \end{cases} \tag{2.7}$$

- Weibull (Type III)

$$G(z) = \begin{cases} e^{-\left[-\left(\frac{z-b}{a}\right)\right]^{\alpha}}, & \text{if } z < b \\ 1, & \text{if } z \geq b \end{cases} \tag{2.8}$$

where $a > 0$ and b (scale and location parameter respectively), are real and the shape parameter α is greater than 0 in the types II and III. Defined as above, G(z) is called Generalized Extreme Value distribution (GEV).
From these results, it follows that the three distribution families characterize different extreme values behaviours. It can be proved that they could be merged into a single family of distribution functions, defined as:

$$G(z) = \begin{cases} exp\left(-\left[1+\theta\frac{z-\mu}{\lambda}\right]^{-\frac{1}{\theta}}\right), & \text{if } \theta \neq 0 \\ exp\left(-exp\left(-\frac{z-\mu}{\lambda}\right)\right), & \text{if } \theta = 0 \end{cases} \tag{2.9}$$

where the location and shape parameters, μ and θ, are finite and the scale parameter λ is positive. The shape parameter can be related to the three types of extreme value distributions as follows:

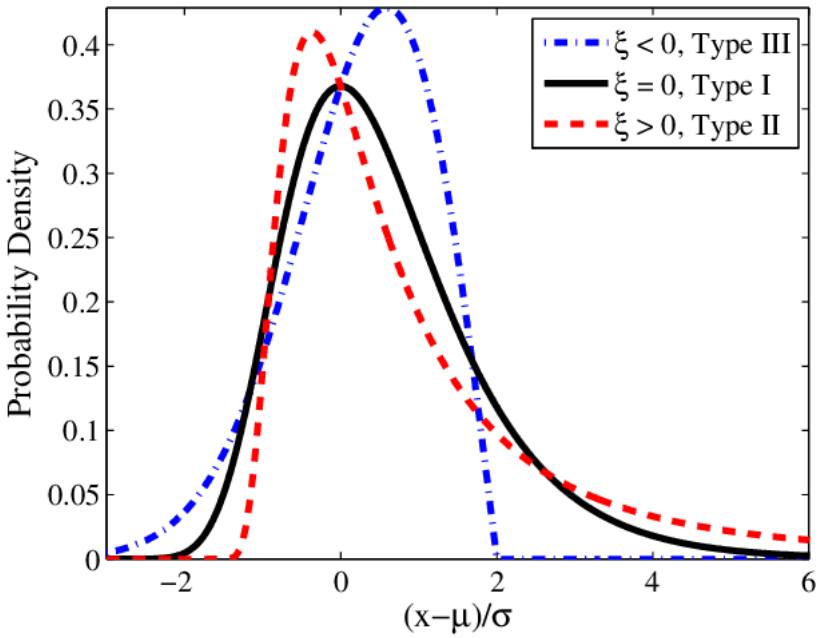

Figure 2.1: The three types of GEV distribution, with normalized sample values on x axis and density probabilities on y axis [Hor et. al, 2008].

- if $\theta = 0$ distribution is type I (Gumbel)
- if $\theta > 0$ distribution is type II (Frechet)
- if $\theta < 0$ distribution is type III (Weibull)

In figure 2.1, the different behaviour of the three families is shown. In the Frechet one, the tail is lower bounded, while in the Weibull one it is upper bounded.

2.2 Metastatistical Extreme Value framework

The Metastatistical Extreme Value framework (MEV) is an approach that assumes the distribution F is known and relaxes the limiting assumptions of the classical EVT. Usually, in real applications, the number of samples is not sufficient for the EVT asymptotic assumption to hold [Cook and Harris, 2004; Koutsoyiannis, 2004]. In MEV, the asymptotic assumption is overcome by explicitly accounting for the yearly number of realizations of the process (n). In doing so, all the ordinary events in the distribution can be used for

estimating the parameters, not only the annual maxima as in the EVT. This procedure drastically reduces the uncertainty in the high-quantiles estimation by up to 50% with respect to the classical theory [Zorzetto et al, 2016].

In particular, MEV considers as random variables

- the parameter defining the number of events (n)
- the parameters of the cumulative distribution function of the event magnitudes(θ, λ)

This leads to a compound distribution for the block maxima. Also, in this framework, the parameters' variability accounts for (i) the randomness of event occurrence which generates a finite and varying number of events in each block and for (ii) the possibly changing probability distribution of event magnitudes across different blocks. To do so, the number of events in each block (n) and the parameters' values (θ, λ) are considered as realizations of stochastic variables (N, Θ, Λ). A graphical representation of this framework is seen in figure 2.2.

Let's now define the MEV cumulative distribution function by considering all possible values of the parameters and the probability distribution of each block maxima:

$$\zeta(x) = \sum_{n=1}^{\infty} \int_{\Omega_{\Theta,\Lambda}} F(x,\theta,\lambda)^n g(n,\theta,\lambda) d\theta d\lambda \tag{2.10}$$

where $g(n,\theta,\lambda)$ is the joint probability distribution of N, Θ, and Λ and $\Omega_{\Theta,\Lambda}$ is the population of all the possible values of the parameters. Accordingly, the probability distribution of the extremes ζ emerges from the full distribution of the ordinary events which is sampled a number of times n every year.

If the expectations are substituted with sample average and the Weibull (stretched-exponential) distribution is adopted for the ordinary events (as usually done for non-zero daily precipitation amounts [Wilson and Tuomi, 2005; Marani and Ignaccolo, 2015]), equation 2.10 becomes

$$\zeta(x) = \sum_{n=1}^{\infty} \int_{\lambda} \int_{\theta} g(n,\theta,\lambda) \left[1 - exp\left(-\left(\frac{x}{\lambda}\right)^{\theta}\right)\right]^n d\theta d\lambda \tag{2.11}$$

where

$$1 - exp\left(-\left(\frac{x}{\lambda}\right)^{\theta}\right) = F(x,\theta,\lambda) \tag{2.12}$$

is the *Weibull distribution* [Weibull, 1951]. A sample of yearly maxima distributions can now be defined, yielding to the sample average approximation

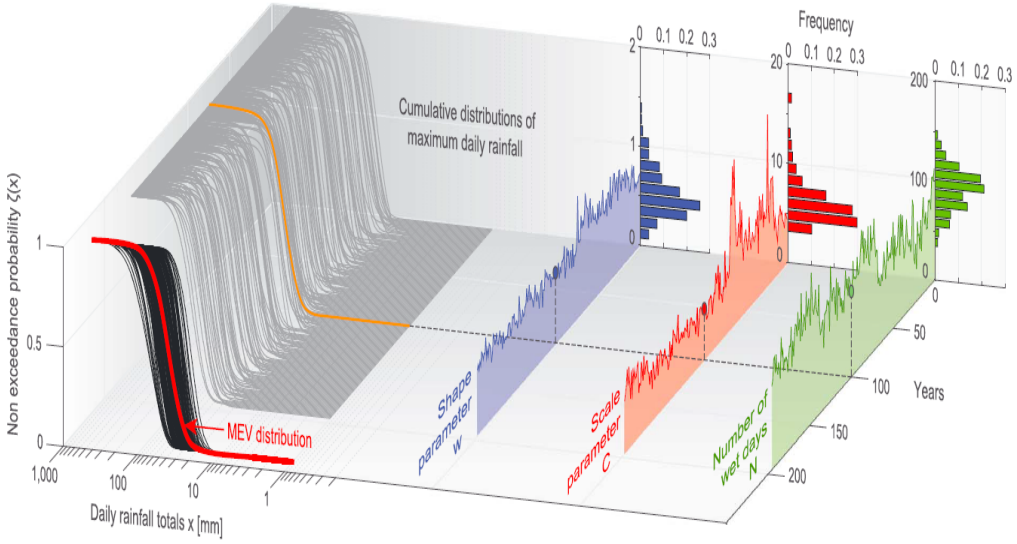

Figure 2.2: A graphical representation of MEV applied to daily rainfall extremes analysis: here the Weibull distribution shape (w in this figure from Zorzetto et al. [2016], θ in this thesis, in blue), scale (C in this figure, λ in this thesis, in red) and number of wet days (N in this figure n in this thesis, in green) are shown in terms of their yearly values and they define the cumulative distributions of maximum yearly rainfall (in gray and black). The MEV distribution (red in the x, y plane) is obtained by means of a sample average over the empirical frequency distribution of the parameters. [Zorzetto et al., 2016]

$\zeta(x) \approx \zeta_m(x)$ so that

$$MEV(x) = \zeta_m(x) = \frac{1}{M} \sum_{j=1}^{M} \left[1 - exp\left(\left(-\frac{x}{\lambda_j} \right)^{\theta_j} \right) \right]^{n_j} \tag{2.13}$$

This is the MEV-Weibull distribution, where j is one of the M total years in record, written as a sample average of the cumulative distribution functions observed during the sampled years.

2.3 The Simplified MEV (SMEV)

One of the main limits of the MEV framework is that, since the number of ordinary events occurring in each year is usually limited, the distribution parameters' estimation may lead to biased values of the quantiles. In particular, the inter-annual variations of the distribution parameters could be due to

- inter-annual variations of the characteristics of the ordinary events
- parameter estimation uncertainty
- variability of different types of ordinary events occurrence

So, in order to overcome these limits, the SMEV, as opposed to MEV, neglects the inter-annual variability in both the ordinary events distributions and in their number of yearly occurrences [Marra et al., 2019b].
Specifically, this means that

1 identical distribution of ordinary events of each type is assumed

2 mean probability of occurrence approximation is applied

The identical distribution assumption, that has been exploited to decrease the parameter estimation uncertainty in latest works [Marra et al., 2019b; Marra et al., 2020], allows to factorize the MEV cumulative distribution function 2.13 in

$$MEV(x) = \prod_{i=1}^{S} \left[F_i(x, \theta_i, \lambda_i)\right]^{n_i} \frac{1}{M} \sum_{j=1}^{M} \left[\prod_{i=1}^{S} \left[F_i\left(x, \theta_i, \lambda_i\right)\right]^{\delta_{i,j}}\right] \tag{2.14}$$

with n_i and $\delta_{i,j} = n_{i,j} - n_i$ respectively expressing the mean number of the i^{th} type of ordinary events occurring in a year and the deviations of the yearly values from the mean. As a consequence, the identical distribution assumption allows to rewrite the term

$$R = \frac{1}{M} \sum_{j=1}^{M} \left[\prod_{i=1}^{S} \left[F_i\left(x, \theta_i, \lambda_i\right)\right]^{\delta_{i,j}}\right] \tag{2.15}$$

as a function of the compound probability without dependence on the distributions F_i and on their parameters. Furthemore, taking the limit $F_i \to 1$, that is the case of extremes, this term becomes negligible in equation 2.14

when estimating return periods exceeding values of the order of 10 years. A new Simplified MEV formulation arises from these results:

$$SMEV(x) = \prod_{i=1}^{S} \left[F_i\left(x, \theta_i, \lambda_i\right)\right]^{n_i} \tag{2.16}$$

This formulation reduces the number of the parameters to $3 \cdot S$ for the Weibull case; also, it gives a direct physical interpretation of them, since n_i is related to the probability of occurrence of the ordinary events of type i, and θ_i and λ_i are related to their intensity. In this work, also the event type variability was neglected, so that equation 2.16 further simplifies, resembling ordinary statistics:

$$SMEV(x) = \left[F\left(x, \theta, \lambda\right)\right]^{n} \tag{2.17}$$

where n is the mean value of ordinary events per year. This is the framework that was adopted in this work: the ordinary events in the distribution tail were used to estimate the extremes' distribution parameters, not all the ordinary events in the distribution as in the usual MEV approach, since, as mentioned in section 1.1.3, it was shown that the tail values are the ones which fit to the Weibull stretched exponential distribution more reliably.

2.3.1 Return period

The return period is the mean representative time interval between two exceedances of a given intensity event. It can be defined as follow [Abarbanel et al., 1992] :

$$RP = \frac{1}{p} \tag{2.18}$$

Since $p = 1 - P(x)$ is the probability of a random variable X having a value greater than x and $P(x) = Pr(X \leq x)$ is an extreme value cumulative probability distribution function (for instance, SMEV), it follows that

$$RP = \frac{1}{1 - P(x)} \tag{2.19}$$

This means that the return period can be directly defined by means of the cumulative distribution function; also, from a more statistical view, it means that in order for the event to happen once, it is necessary to make, on average, 1/p trials.

2.3.2 Return levels

When studying precipitation extremes, it is useful to derive and analyze the corresponding return levels or quantiles.

If q is the return level (or quantile) associated to the return period $1/P$, then, recalling the return period definition, its value could be exceeded (on average) every year with probability P. Commonly, it is referred to as the return level which is expected to be exceeded once every $1/P$ years.

For the case of SMEV used in this work, the equation used for retrieving quantiles is

$$q = \lambda \left[-ln \left(1 - P^{\frac{1}{n}} \right) \right]^{\frac{1}{\theta}} ; \tag{2.20}$$

with λ and θ being the scale and shape parameters of the Weibull distribution, respectively, P the cumulative distribution function like in section 2.3.1, so that

$$P = 1 - \frac{1}{RP}, \tag{2.21}$$

and n the mean number of ordinary events per year.

Chapter 3

Data

3.1 Study Areas

The selection of the study areas has been influenced by the needs of having

a Ground-based reliable and relatively long measurements to be used as a benchmark

b Regions with different climatic conditions

Combining these two fundamental aspects, a dense network of stations in a region of south-eastern Austria and a more sparse network covering Israel were selected.

These study cases have different characteristics: the first dataset includes a small homogeneous area which is classified as warm-summer humid continental climate Dfb [Koppen and Geiger, 1936], so no dry season can be effectively identified and the monthly average temperature is always below $22°C$; the second region, instead, could be divided into three main climate types, which are

- Csa: Warm mediterranean climate
- BSh: Warm semi-arid climate
- BWh: Warm desert climate

with monthly average temperatures often exceeding $22°C$ (figure 3.1). Moreover, more or less long dry time intervals could be identified depending on the region. Since the differences between the BSh and BWh are slight and the network in these areas is relatively sparse, in this work, these areas are considered as one: the latitude of $31.5°N$ was chosen to separate a

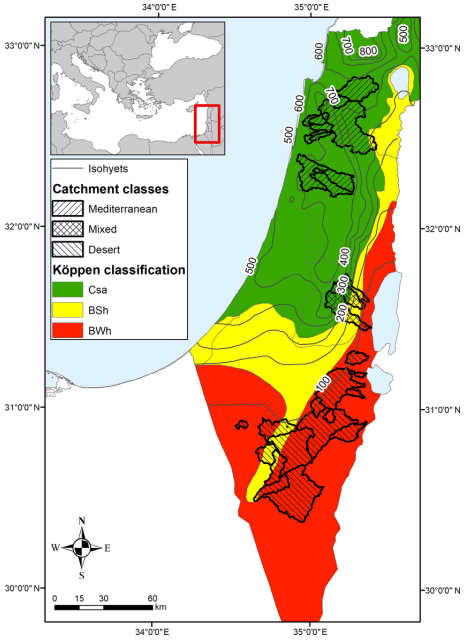

Figure 3.1: Climatic zones of Israel. [Zoccatelli et al., 2019]

"Mediterranean" region (which includes the area classified as Csa) from an "Arid" one (roughly BSh and BWh areas). Thus, three main climatic zones were identified and studied on the basis of the selected areas.

3.2 Stations

3.2.1 Austria

The selected stations are part of the WegenerNet network: a very dense ensemble of stations which covers the surroundings of Feldbach in the Styria region. A graphical overview of the stations' distribution can be seen in figure 3.2. The 151 considered stations provide daily precipitation data of the *last* 24 hours (in mm), with a detection threshold of 0.11 mm, initialized at every 12:00 UTC, from 2007 to the end of 2020 [Fuchsberger et al., 2021].

It is crucial to highlight that this network was created to be independent from satellite-based precipitation products, which means that these data are *not* used for adjusting the satellite data.

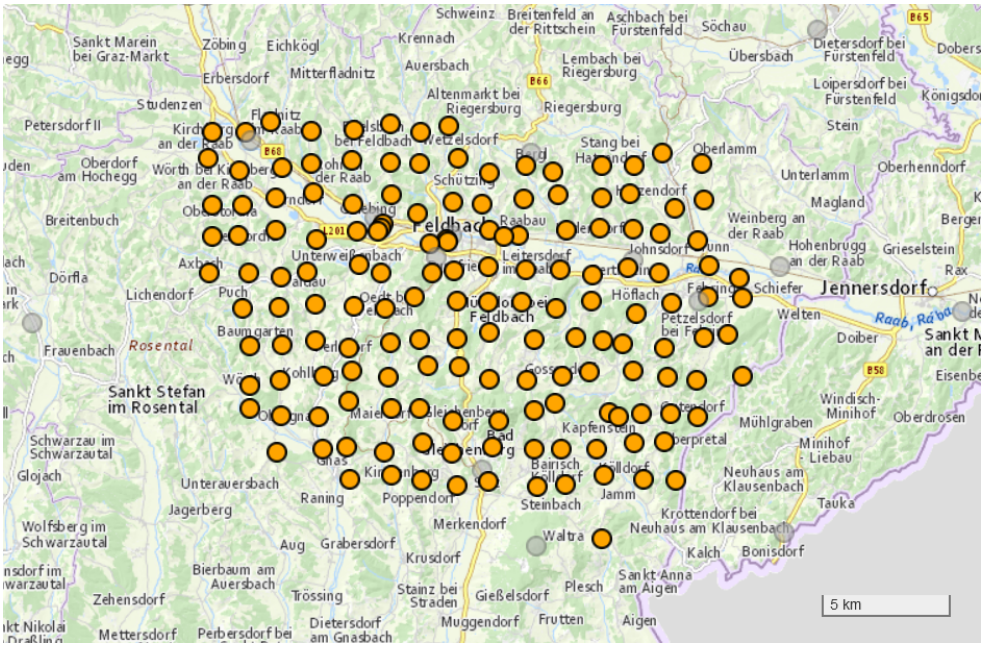

Figure 3.2: Spatial distribution of WegenerNet network stations in the Feldbach surroundings (Austria) [WegenerNet DataPortal].

Quality control

Preliminary data quality control was carried out seeking for

1 Missing values

2 Missing years

Missing values are expected to be stored as NA or -9999, but Austria stations did not show any missing data, also due to interpolation. Some of the 151 stations were deleted from the final dataset, since they were characterized by the absence of one or more yearly records, thus leading to a total of 128 out of 151 reliable daily rain records.

Furthermore, in the data, a flag, showing the percentage of interpolated precipitation values was also reported: preliminary tests were made to understand whether this type of data should be considered, and so censoring the precipitation records with an interpolated value greater than a predefined threshold, or not. Also, interpolated data could report values below the gauges' detection threshold of 0.11 mm. Results showed that the years with more than 10% of interpolated values are more than 20% of the total. Since this would lead to a conspicuous loss of data, interpolated precipitation values also were considered in the following analyses.

3.2.2 Israel

Israel data were extracted from 408 rain gauges distributed heterogeneously. The data temporal coverage is also uneven, in fact they vary from year 1948 to 2018 and several stations reported them in different yearly length records. This is another difference to be analyzed with respect to the Austrian case. Israeli data report all the recorded daily precipitation values of the $following$ 24 hours, initialized at every 06:00 UTC, greater or equal to the minimum detectable magnitude of 0.1 mm.

In this case, only ten (out of 408) stations are exploited for calibration of satellite-based precipitation retrievals.

Quality control

Israel stations data were already filtered for missing values [Marra et al., 2021]. Years with more than 10% missing data were removed from the analyses.

3.3 Satellite

Satellite data were taken from the 6^{th} version of the Integrated Multi-satellitE Retrievals algorithm (IMERG) of the Global Precipitation Measurement mission (GPM) [Huffman et al., 2015]. IMERG combines precipitation estimates from microwave and infrared radiance-based observations from geosynchronous satellites [Joyce and Xie, 2011] and combines them with space-borne radars from the GPM core satellites and rain gauges [Hou et al., 2014; Hong et al., 2004; Huffman et al., 2007; Rudolph and Schneider, 2015]. This new release allows to merge early precipitation data collected by the previous Tropical Rainfall Measuring Mission (TRMM) [Simpson et al., 1996], during the 2000-2014 period, with recent estimates obtained by the GPM satellite constellation from 2015 to present day in order to obtain a relatively long dataset. The reader interested in more information on the improvements of this new algorithm is referred to Tan et al. [2018]. The estimates cover portions of the globe between 90° N-S of latitude on a 0.1° x 0.1° grid, updated every 30 minutes and reported in mm/h.

Specifically, the IMERG "final run" is used, which includes the most updated and quality-controlled estimates. The R package *ncdf4* version 1.17 was used to open and read the downloaded files which are in the HDF5 format. After opening one of these half-hourly files, as visible in listing 3.1, four variables can be identified and analyzed:

- Precipitation estimate in mm/h ("PrecipitationCal")
- Time step in seconds ("time")
- Latitude ("lat")
- Longitude ("lon")

```
1
2  File C:/Imerg/IMERG_V06_HH_NorthItaly/2020/
3         3B_HHR.MS.MRG.3IMERG.20200105_
4         S033000_E035959.0210.V06B.HDF5.nc4
5         (NC_FORMAT_NETCDF4_CLASSIC):
6
7       1 variables (excluding dimension variables):
8          float precipitationCal[lat,lon,time]
9              DimensionNames: time,lon,lat
10             Units: mm/hr
11             units: mm/hr
12             coordinates: time lon lat
13             _FillValue: -9999.900390625
14             CodeMissingValue: -9999.9
15             origname: precipitationCal
16             fullnamepath: /Grid/precipitationCal
17
18      3 dimensions:
19         time  Size:1
20             DimensionNames: time
21             Units: seconds since 1970-01-01 00:00:00 UTC
22             units: seconds since 1970-01-01 00:00:00 UTC
23             standard_name: time
24             LongName: Representative time of data in
25       seconds since 1970-01-01 00:00:00 UTC.
26             bounds: time_bnds
27             axis: T
28             calendar: julian
29             origname: time
30             fullnamepath: /Grid/time
31         lon  Size:121
32             DimensionNames: lon
33             Units: degrees_east
34             units: degrees_east
35             standard_name: longitude
36             LongName: Longitude at the center of
37       0.10 degree grid intervals of longitude
38       from -180 to 180.
39             bounds: lon_bnds
40             axis: X
```

```
            orignname: lon
            fullnamepath: /Grid/lon
        lat  Size:71
            DimensionNames: lat
            Units: degrees_north
            units: degrees_north
            standard_name: latitude
            LongName: Latitude at the center of
      0.10 degree grid intervals of latitude
      from -90 to 90.
            bounds: lat_bnds
            axis: Y
            orignname: lat
            fullnamepath: /Grid/lat

    6 global attributes:
        FileHeader: DOI=10.5067/GPM/IMERG/3B-HH/06;
DOIauthority=http://dx.doi.org/;
DOIshortName=3IMERGHH;
AlgorithmID=3IMERGHH;
AlgorithmVersion=3IMERGH_6.3;
FileName=3B-HHR.MS.MRG.3IMERG.20200105-S033000-E035959
         .0210.V06B.HDF5;
SatelliteName=MULTI;
InstrumentName=MERGED;
GenerationDateTime=2020-05-04T06:58:52.000Z;
StartGranuleDateTime=2020-01-05T03:30:00.000Z;
StopGranuleDateTime=2020-01-05T03:59:59.999Z;
GranuleNumber=;
NumberOfSwaths=0;
NumberOfGrids=1;
GranuleStart=;
TimeInterval=HALF_HOUR;
ProcessingSystem=PPS;
ProductVersion=V06B;
EmptyGranule=NOT_EMPTY;
MissingData=;

        FileInfo: DataFormatVersion=6a;
TKCodeBuildVersion=0;
MetadataVersion=6a;
FormatPackage=HDF5-1.8.9;
BlueprintFilename=GPM.V6.3IMERGHH.blueprint.xml;
BlueprintVersion=BV_62;
TKIOVersion=3.93;
MetadataStyle=PVL;
EndianType=LITTLE_ENDIAN;

        Grid.GridHeader: BinMethod=ARITHMETIC_MEAN;
```

```
Registration=CENTER;
LatitudeResolution=0.1;
LongitudeResolution=0.1;
NorthBoundingCoordinate=90;
SouthBoundingCoordinate=-90;
EastBoundingCoordinate=180;
WestBoundingCoordinate=$-$180;
Origin=SOUTHWEST;

        Grid.fullnamepath: /Grid
        DODS_EXTRA.Unlimited_Dimension: Grid_time
        history: 2021-04-21 04:19:47 GMT Hyrax-1.15.4
        https://gpm1.gesdisc.eosdis.nasa.gov/opendap/GPM_L3/
        GPM_3IMERGHH.06/2020/005/3B_HHR.MS.MRG.3IMERG
    .20200105
        _S033000_E035959.0210.V06B.HDF5.nc4?
        precipitationCal[0:0][1859:1979][1329:1399],
        time,lon[1859:1979],lat[1329:1399]
```

Listing 3.1: Example of half-hourly IMERG HDF5 file as opened with R ncdf4 package

The first coordinate, *time*, that is the recording time in seconds since 1970/01/01 00:00 UTC, has been transformed into day/month/year and hour/minutes/seconds info. The second and the third variables, *lon* and *lat*, represent the longitude and latitude at the center of the 0.1° grid cells and are characterized by 121 and 71 values respectively for the "NorthItaly" observing area data (ranging from 5.95° W to 17.95° W in longitude and from 42.95° N to 49.95° N in latitude), that include several countries, among which Austria. For the Israel observing area, the *lon* and *lat* dimensions are characterized by 91 and 81 values (ranging from 32.05° W to 40.05° W and from 26.95° N to 35.95° N).

3.3.1 Pixel selection

The satellite pixels (i.e. the grid cells) including the coordinates of the analyzed rain gauges for both areas needed to be identified. In fact, only a small number of pixels was used, because of the facts that the starting HDF5 data report values on relatively wide areas and that every grid cell includes more than one station. Analyzing the stations' latitude and longitude coordinates, a match between these values and those of the corresponding grid cells centers was made so as to select and associate the pixels to be used to the right stations. This match was considered as correct if a station was within ±0.05° both in latitude and longitude from those of the specified satellite pixel's center. In table 3.1, the number of the selected pixels and their minimum and

maximum latitude and longitude values are reported.

	Austria	Israel
N. of pixels	8	143
Lat min	46.85°	29.55°
Lat max	46.95°	33.25°
Lon min	15.75°	34.35°
Lon max	16.05°	35.85°

Table 3.1: Number of extracted satellite pixels and their maximum and minimum center coordinates values.

3.3.2 Filtering and Aggregation

Satellite precipitation estimates are available every 30 minutes, while station data directly report daily cumulated values. Thus, satellite estimates were aggregated to the corresponding temporal scales. To achieve this goal, two preliminary conversions were applied:

1 Half-hourly precipitation intensities (mm/h) into half-hourly precipitation accumulations (mm), assuming uniform precipitation rate during the 30-min time intervals

2 Time step in seconds into time step in year/month/day hh/mm/ss

Then, before starting the aggregation, missing value records labeled with NA were either set to zero, if limited to ≤ 6 hours per day , or else deleted.Merging of the half hourly satellite data, for both areas, was done, taking into account that the initializing time for rain-gauges is 12:00 UTC for Austria and 6:00 UTC for Israel, while, for IMERG data, values are saved as precipitation estimates in the 30 minutes following the time step.

Chapter 4

Methods

After having filtered data, several analyses were carried on as described in this chapter. In section 4.1, the ordinary events identification process is described, followed by the identification of the distribution tail (section 4.2). Parameters' estimation (still section 4.2) is described before high return period quantiles' estimation (section 4.3). Then, differences between rain gauge stations and IMERG estimates (defined as errors) were studied and error propagation was applied so as to see how the observed differences matched with series expansions (section 4.4) to point out and quantify reliability of the satellite product. Last, the correlation between the first two moments of the distribution and the estimated parameters was studied (section 4.5), in order to find out how already available information, such as statistics of the satellite estimation errors, could be related to biases in the SMEV parameters, and consequently in the quantiles.

4.1 Ordinary events identification

4.1.1 Austria

Ordinary events, here considered as independent wet days (refer to section 1.1.3 for a definition), were identified. A precipitation threshold, expressed in mm/day, was chosen in order to define the wet days. Cross-check using the satellite data showed an optimal agreement in the detection of the number of wet days. For the case of Austria, all daily amounts greater or equal than 0.1 mm were defined as wet, since stations and satellite showed a good match.

4.1.2 Israel

Comparison with satellite data showed a not negligible difference in detection of the number of yearly wet days according to the precipitation daily threshold. In fact, based on figures 4.1 and 4.2, the 1 mm threshold was chosen, since, close to that value, n becomes comparable for the two products. Furthermore, it can be noticed that the Mediterranean (MED) stations, which are roughly 90% of the total (367/408), are those which weigh more on the variability of the median value of the mean number of events. The Arid stations (ARID) show more overestimation for satellite data and very high dispersion, as pointed out by the 5th and 95th percentile trend, but, since they represent 10% of the stations only, they affect the overall behaviour only slightly.

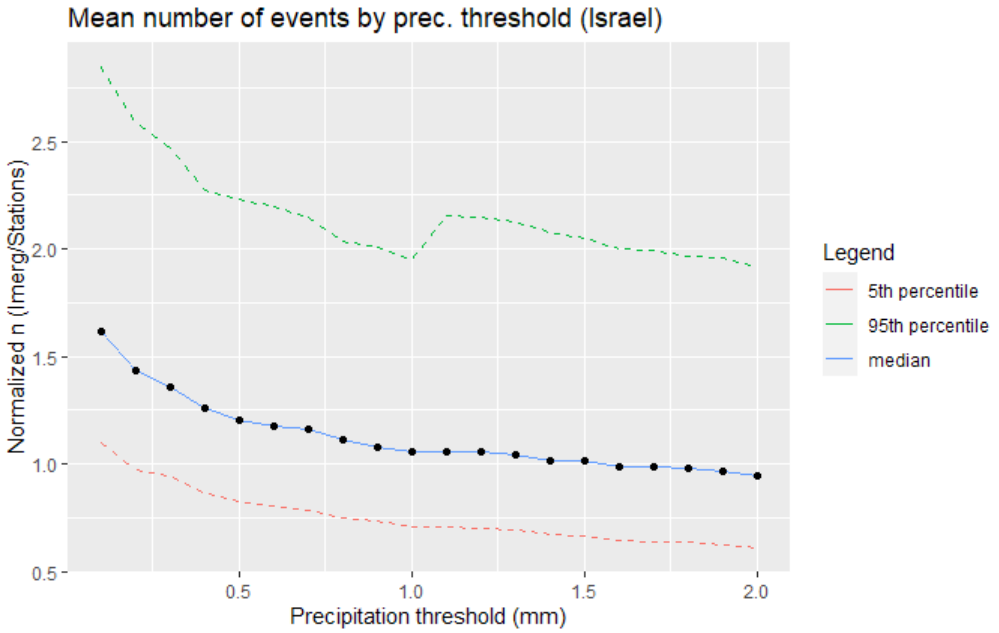

Figure 4.1: Bias (IMERG/Stations) in the mean number of yearly events estimated using daily precipitation thresholds based on all satellite and stations filtered values

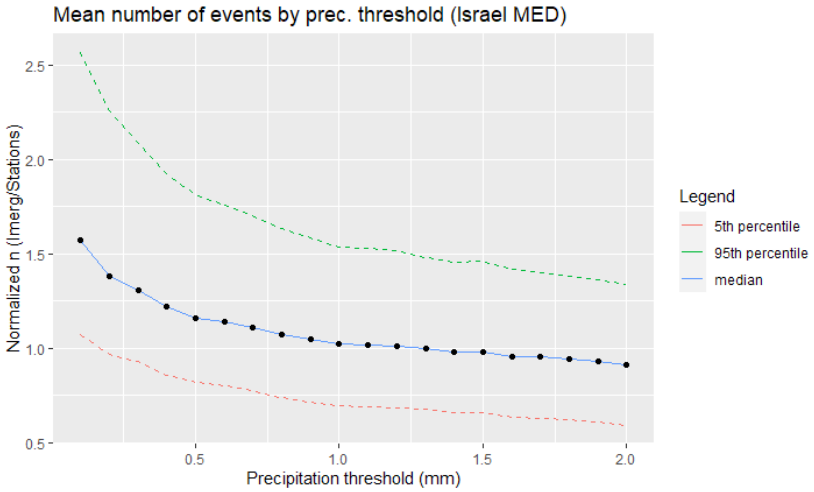

(a) MED

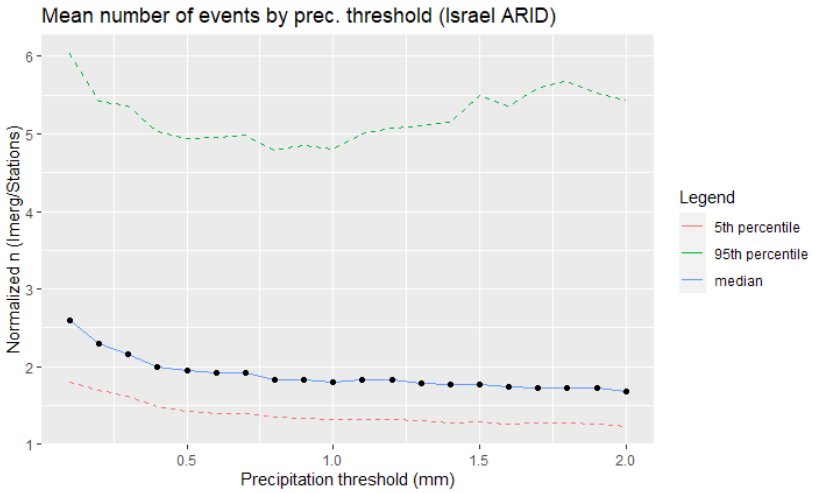

(b) ARID

Figure 4.2: Bias (IMERG/Stations) in the mean number of yearly events estimated using daily precipitation thresholds based on all satellite and stations filtered values: (a) Mean n for the mediterranean stations. (b) Mean n for the arid stations.

4.2 Distribution tail identification

Following section 4.1, the *tail* of the ordinary events distribution, which is the portion related to the most intense samples for which the assumption of Weibull-tail holds, had to be identified. A test [Marra et al, 2020] was implemented and applied to the rain gauge data, since considered as the reference, to identify the portion of the ordinary events' distribution better adapting to a Weibull stretched exponential cumulative distribution function (eq. 2.12).

4.2.1 Weibull tail test

A main function, called *test SMEV* was implemented in *R* programming language to apply the test mentioned above. The six inputs of the function are: *vals* (the precipitation ordinary events), *bids* (the recording year of each vals), *data portion* (the portion of the events' distribution to consider), *p* (probability value between 0 and 1 related to the confidence interval), *niter* (number of iterations) and *station* (the analyzed rain gauge station ID number).

In the first part of the script, the ordinary events are sorted from the smallest to the largest along with their bids, then annual maxima are identified and flagged.

Subsequently, two functions, *Weibull fit* and *random weibull* are called in the script, which, respectively, allow to: estimate the ordinary events' distribution parameters according to a given definition of the tail, and to randomly generate a number *niter* of Weibull-distributed samples. The *Weibull fit* script is described later in this section.

As shown in listing 4.1, at line 34 the Weibull tail test is applied to the events' distribution: annual maxima are selected and then compared to those of 1000 random Weibull distributions created by bootstrap with replacement (*random weibull function*). Quantiles of the randomly generated array are computed by means of the *quantile* function, with $p/2$ and $1 - p/2$ denoting the probabilities of the lower and upper percentile of the confidence interval.

If 80% confidence interval is selected, then $p = 0.2$ and the two test variables, *p hi* and *p low*, give the mean fraction of the samples' annual maxima that are higher or lower than the 90th and the 10th percentile of the 1000 Weibull synthetic distributions. If *p out* = *p hi* + *p low* is lower than 0.2, i.e. if less than 20% of the maxima are out of the confidence interval, the sample values can be considered as likely samples from Weibull-distributed ordinary events.

According to the adopted confidence interval metrics, this means that

the analyzed portion of the events' distribution can be well described by a Weibull one. Else, if $p\ out > 0.2$, the assumption of having a Weibull tail defined by the used data portion is to be rejected.

```
test_SMEV <- function(vals,bids,data_portion,p,niter,station)
{
  #let's sort the ordinary events
  bids <- bids[order(vals)]
  vals <- sort(vals)

  #here i put a flag on the annual maxima
  isams <- matrix(0, ncol=1, nrow=length(vals))
  for (id in unique(bids)) ##devo trasporlo?
  {
    ams <- 0
    for (l in  which((bids==id)!=0))
    {
      if(vals[l]>ams)
      {
        ams <- vals[l]
        iams <- l
      }
    }
    isams[iams] <- 1
  }
  ------------------------------------------------------
  #calling the function wich estimates the distribution
   parameters
  parameters <- weibull_fit(vals,data_portion,isams,censorams
    = TRUE,station)


  #creation of an array of random weibull distributions
  randy <- random_weibull(niter,parameters[,1],parameters
   [,2],length(vals))
  ------------------------------------------------------
  istest <- isams
  ##Here, test to verify tail beahaviour is applied
  p_lo <- mean(vals[istest==1] < apply( randy[,istest==1] , 2
    , quantile , probs = p/2 , na.rm = TRUE ),na.rm = TRUE)
  p_hi <- mean(vals[istest==1] > apply( randy[,istest==1] , 2
    , quantile , probs = 1-p/2 , na.rm = TRUE ),na.rm = TRUE)

  p_out <- p_hi + p_lo
  results <- data.frame(p_lo,p_hi,p_out)
  return(results)
}
```

Listing 4.1: SMEV test function code

Weibull fit function: parameter estimation

In this script (see listing 4.2), which can be applied to both land and satellite based data, the distribution parameters are estimated by taking as input the ordinary events and the selected data portion to be analyzed. In the beginning, if input data are not ranked up from the smallest to the largest, data sorting is applied. Then, the Empirical Cumulative Distribution Function (ECDF), which gives the empirical non exceedance probability, is computed by using the Weibull plotting positions formula and the section of sample values is selected on the basis of the data portion input. Subsequently, if the function is called by the *test SMEV*, annual maxima are censored from the data in order to have independence for the tail test.

Afterwards, coordinates transformation is applied to data (ordinary events and ECDF), in order to derive the distribution parameters n, λ, θ by means of a linear regression. Last, a linear Weibull fit is plotted on the selected portion of the ordinary events distribution according to the estimated parameters, in order to visually appreciate the match between the estimated Weibull distribution and the available data samples.

```
1  weibull_fit <- function(data_nozero, data_portion,isams,
2                          censorams,station)
3  {
4     #We start by sorting in ascending order the input (non
5     #zero) data
6     X <- sort(data_nozero, decreasing = FALSE)
7     ib <- order(data_nozero)
8     isams <- isams[ib]  #here the position of the ordered data
9     #in the original vector (data_nozero) is declared
10
11    ECDF <- matrix(data= ((1:length(X))/(length(X)+1)))
12    fidx <- max(1,trunc(length(X)*data_portion[1]))
13    tidx <- ceiling(length(X)*data_portion[2])
14    to_use <- fidx:tidx
15
16    #annual maxima censoring
17    if (censorams==TRUE)
18    {
19      to_use <- to_use[is.element(to_use,which(isams==0))]
20    }
21    #variables transformation
22    t <- log(log(1/(1-ECDF[to_use])))
23    u <- log(X[to_use])
24    v <- matrix(1, nrow = length(X[to_use])) #weight matrix
25    res_vec <- data.frame(t,u,v)
26    ----------------------------------------------------
27    Results <- weightedfit(res_vec)
```

```
28    shape <- 1/Results[,1] #Results[,1] is the slope
29    scale <- exp(Results[,2])#Results[,2] is the intercept
30    parameters <- data.frame(shape,scale)
31
32    #Ordinary events distribution and Weibull fit plot
33    plot1 <- ggplot(data=NULL)+
34             geom_point(mapping=aes(x=t,y=u)) +
35             geom_line(mapping = aes(x=t,y=Results[,1]*t+
36             Results[,2]), col='red') +
37             labs(y= "log(DailyRain)", x = "log(log(1/
38             Exceedance probability)",title = str_c('Weibull
39             Fitting Station ',station), subtitle= str_c('
40             Lower limit = ', data_portion[1]) )
41    show(plot1)
42
43    return(parameters)
44 }
45 ----------------------------------------------------------
46 weightedfit <- function (data)
47               {
48                x <- data[,1]
49                y <- data[,2]
50                dimensions <- dim(data)
51                s <- dimensions[1]
52                t <- dimensions[2]
53                stdv <- matrix(1, nrow = s)
54                if (t==3)
55                {
56                  stdv <- data[,3]
57                }
58                w <- 1 / stdv^2
59                S <- sum(w)
60                Sx <- sum(w*x)
61                Sy <- sum(w*y)
62                Sxx <- sum(w*(x^2))
63                Sxy <- sum(w*x*y)
64                Delta <- S*Sxx - (Sx)^2
65                a <- (Sxx*Sy - Sx*Sxy) / Delta
66                b <- (S*Sxy - Sx*Sy) / Delta
67
68                Results_slope <- b
69                Results_intercept <- a
70                results_weighted <- data.frame(Results_slope,
71                                               Results_intercept)
72
73                return(results_weighted)
74               }
```

Listing 4.2: Weibull fit function code

4.3 Quantiles computation

After tail identification and parameters estimation, distribution quantiles with long return period, for both rain gauges and satellite data, can be computed.Quantiles associated to 2, 5, 10, 50, 100 and 500 years return periods are computed using the inversion formula defined in section 2.3.2.

4.4 Error estimation and propagation

Differences between IMERG and rain gauge based estimated parameters and quantiles were defined as *errors*. Scatter plots were used to visually inspect these errors, in order to see which device showed overestimation or underestimation with respect to the other.

Then, the propagation of the error from satellite precipitation estimates to SMEV-estimated quantiles was derived using Taylor series expansions. Observed and estimated normalized errors in the quantiles were compared, with IMERG values treated as deviations from reference values (rain gauges).

If second order series expansion is applied, then the deviation δq is

$$\begin{aligned}\delta q = q(Sat) - q(Stat) = \left(\frac{dq}{d\lambda}\right)\delta\lambda + \left(\frac{dq}{d\theta}\right)\delta\theta + \left(\frac{dq}{dn}\right)\delta n + \\ + \frac{1}{2}\left[\left(\frac{d^2q}{d\lambda^2}\right)\delta\lambda^2 + \left(\frac{d^2q}{d\theta^2}\right)\delta\theta^2 + \left(\frac{d^2q}{dn^2}\right)\delta n^2\right]\end{aligned} \tag{4.1}$$

where $\delta\lambda$, $\delta\theta$ and δn are the satellite parameters errors.

It should be highlighted that the series expansion is well applicable to relatively small errors, while greater deviations are expected for higher ones.

First derivatives

If quantiles are determined through equation 2.20, *first derivatives* are such that

$$\begin{aligned}
\frac{dq}{d\lambda}\delta\lambda = dq|_{\lambda} &= \left[-ln\left(1-P^{\frac{1}{n}}\right)\right]^{\frac{1}{\theta}}\delta\lambda = q\frac{\delta\lambda}{\lambda} \\
\frac{dq}{dn}\delta n = dq|_{n} &= \frac{\lambda}{\theta}\left[-ln\left(1-P^{\frac{1}{n}}\right)\right]^{\frac{1-\theta}{\theta}}\left[\frac{P^{\frac{1}{n}}ln(P)}{n^2-n^2P^{\frac{1}{n}}}\right]\delta n = \\
&= \frac{q}{\theta}\frac{\lambda}{q}\left[\frac{P^{\frac{1}{n}}ln(P)}{n^2-n^2P^{\frac{1}{n}}}\right]\delta n \\
\frac{dq}{d\theta}\delta\theta = dq|_{\theta} &= -\frac{\lambda}{\theta^2}\left[-ln\left(1-P^{\frac{1}{n}}\right)\right]^{\frac{1}{\theta}}ln\left[-ln\left(1-P^{\frac{1}{n}}\right)\right]\delta\theta = \\
&= -\frac{q}{\theta^2}ln\left[\left(\frac{q}{\lambda}\right)^{\theta}\right]\delta\theta
\end{aligned} \tag{4.2}$$

thus

$$\frac{dq|_{\lambda}}{q} = \frac{\delta\lambda}{\lambda} \tag{4.3}$$

$$\frac{dq|_{n}}{q} = \frac{\lambda}{q\theta n}\left[\frac{P^{\frac{1}{n}}ln(P)}{1-P^{\frac{1}{n}}}\right]\frac{\delta n}{n} \xrightarrow[P\to 1]{} -\frac{\lambda}{\theta q}\frac{\delta n}{n} \tag{4.4}$$

$$\frac{dq|_{\theta}}{q} = -\frac{ln\left[\left(\frac{q}{\lambda}\right)^{\theta}\right]}{\theta}\frac{\delta\theta}{\theta} \tag{4.5}$$

These are the equations adopted in the error computation analysis for the first order expansion. As it can be noticed, the second one simplifies into a more handy expression if P tends to 1, that is the case of high return period (extreme) quantiles.

The match between observed and estimated errors is expected to improve for higher quantiles, due to the presence of the variable P in the quantile estimation equation.

Second derivatives

Considering the definitions obtained for the first derivatives, the second order expressions are such that

$$\frac{dq^2}{d\lambda^2}\delta\lambda^2 = dq^2|_\lambda = 0$$

$$\frac{dq^2}{dn^2}\delta n^2 = dq^2|_n = -\frac{\lambda p^{\frac{1}{n}} ln(p)\left(\frac{q}{\lambda}\right)^{1-2\theta}}{\theta^2 n^2\left(p^{\frac{1}{n}}-1\right)^2}\cdot \cdot\left\{ln(p)\left[(\theta-1)\,p^{\frac{1}{n}} - \theta\left(\frac{q}{\lambda}\right)^{\theta}\right] + 2\theta n\left(p^{\frac{1}{n}}-1\right)\left(\frac{q}{\lambda}\right)^{\theta}\right\}$$

$$\frac{dq^2}{d\theta^2}\delta\theta^2 = dq^2|_\theta = \frac{qln\left[\left(\frac{q}{\lambda}\right)^{\theta}\right]\left\{2\theta + ln\left[\left(\frac{q}{\lambda}\right)^{\theta}\right]\right\}}{\theta^4}\delta\theta^2 \tag{4.6}$$

For P $\rightarrow$1 the second equation tends to 0, so both the *scale* and n parameters contributions to the second order expansion can be neglected. Thus, the term

$$\frac{d\theta^2|_\theta}{\theta} = \frac{qln\left[\left(\frac{q}{\lambda}\right)^{\theta}\right]\left\{2\theta + ln\left[\left(\frac{q}{\lambda}\right)^{\theta}\right]\right\}}{\theta^5}\delta\theta^2 \tag{4.7}$$

is the only second order one which influences the series expansion. These results show that the biggest weight in error propagation is due to the observed shape deviations.

4.5 Moments-parameters correlation

Analysing the correlation between the derived parameters and the first moments of the ordinary events distribution allows us to understand how derived information directly related to the errors in the estimated extreme quantiles, such as the errors in the parameters, could be related to quantities (moments) that can be directly obtained from prior knowledge of the ordinary events' distribution and of the satellite estimation errors. This investigation could help for associating the results gained in this work with preliminary information on the accuracy of satellite data, even regarding other regions of the globe.

Specifically, after having identified the left data portion which defines the distribution tail, bias of the estimated *shape* and *scale* parameters (IMERG/S-tations) were plotted against:

- bias in the mean of the values above the selected threshold
- bias in the standard deviation of the values above the selected threshold

In the case of Israel, the correlation was studied both considering all the sites together and dividing them according to the two climatic zones.

Chapter 5

Results

In this chapter, the main results obtained by applying the methods discussed in chapter 4 to the Austrian and Israeli land and satellite based data are presented.

Starting from the identification of the distribution tails, several plots were made and reported to see the correlations and differences in distribution parameters and estimated quantiles between the two instruments in the three climatic areas.

5.1 Distribution tail

Recalling section 4.2, in order to identify the distribution tails, the Weibull tail test was applied to several portions of each station's ordinary events distribution, both for Austria and Israel.

Histograms (figure 5.1) were made to identify which part of the distribution shows a Weibull behaviour. The bins' values represent the first left data portion threshold, starting from the end of the distribution, for which the value of $p\ out = p\ hi + p\ low$ (where $p\ hi$ and $p\ low$ give the mean fraction of the samples' annual maxima that are higher or lower than the 90th and the 10th percentile of the 1000 Weibull randomly generated distributions if a confidence interval of 80% is selected) of the considered station falls below 0.2.

Furthermore, after having identified the optimal thresholds, linear fits of the Weibull distributions describing the tail, computed by means of the selected data portion parameters, were plotted on the overall ordinary events distributions for better visual evaluation (figure 5.2).

Austria

By looking at figure 5.1 (a), the tail of the distribution was identified as the highest 10% values: in fact, once passed the 0.9 left threshold, most of the stations had already reached *p out* values below 0.2.

Specifically, 75% of the 128 analyzed stations show *p out* values that, at some point, are smaller than 0.2; moreover, for 82% of these, it happens between 0 and 0.9 thresholds. This value of 0.9 is in agreement with the other studies [Miniussi and Marra, 2021] based on data from Germany, where the climatic conditions usually characterized by stratiform precipitation are similar to those of Austria. Figure 5.2 (a) shows what happens if the linear Weibull fit, computed by exploiting this portion of data for which *p out* falls below 0.2 for the first time without increasing again, is overlaid on the overall distribution of a station in transformed coordinates. The Weibull fit based on the highest 10% ordinary events values matches that portion of the distribution, while it departs from them at lower values, corroborating the choice of 0.9 as left data portion threshold for Austria ordinary events distribution tail identification. This choice implies that, in Austria, the annual maximum daily precipitation amounts are likely samples from ordinary events with Weibull tail, defined as the largest 10% of the ordinary events.

Israel

In Israel (figure 5.1 (b)), the selected left data portion threshold is 0.75. In fact 98% of the 408 analyzed stations showed values of *p out* below 0.2 at some point of the distribution and for 87% of these it happens before the 0.75 threshold included. This is in agreement with other precipitation frequency analysis works studying data from this Israeli stations network [Marra et al., 2019b].

As shown in figure 5.2 (b), the 25% most intense precipitation values fit well the linear Weibull distribution with progressive deviation for lower values. It can be noted that, in the y axis, values of the logarithm of daily precipitation start from a higher magnitude than those of Austria (figure 5.2 (a)): this is due to the fact that the chosen precipitation threshold is 1 mm for Israel, as opposed to the 0.11 mm of Austria, thus leading to a censoring of low ordinary events values. Also, the overall shape of the distribution is different from that of the Austrian stations: in fact, lower ordinary events show a lower deviation from the Weibull fit. This can be explained by considering that in Israel the precipitation events are more easily related to convective structures, thus more likely to be independent and Weibull distributed [Wilson and Tuomi, 2005; Berg et al., 2013].

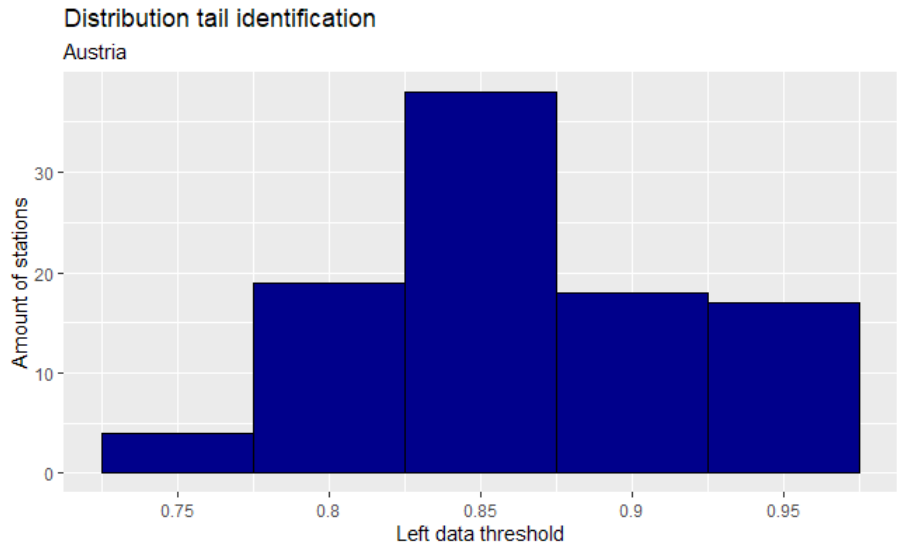

(a) Austria

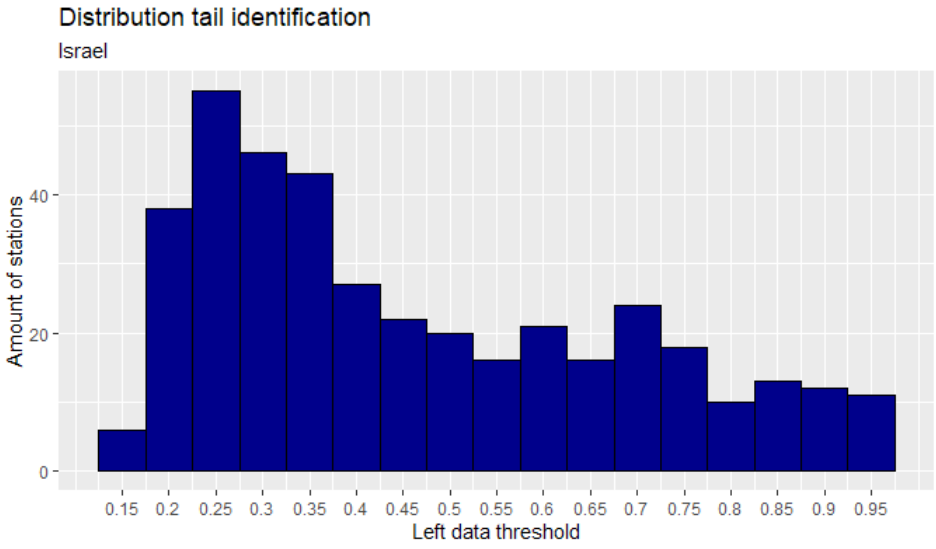

(b) Israel

Figure 5.1: Austria and Israel *p out* histograms for distribution tail identification: each bin represents the left data portion threshold for which, for the first time, starting from right, the value of *p out* in the Weibull tail test falls below 0.2 without increasing again above that value until the end of the distribution. On the x axis, the left data portion threshold is reported by means of normalized interval (0,1).

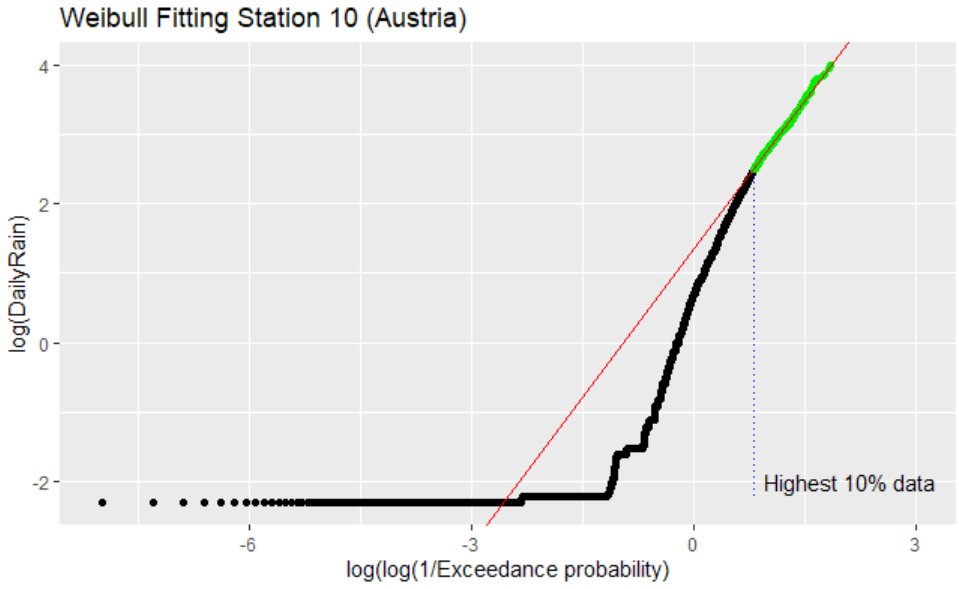

(a) Austria

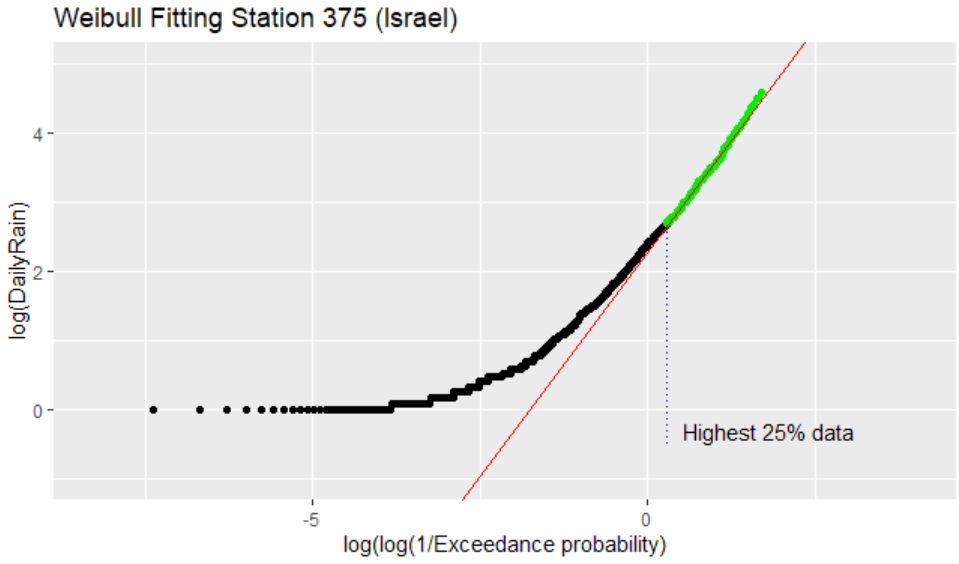

(b) Israel

Figure 5.2: Weibull fits (red line) obtained from 0.9 and 0.75 left data portion threshold for Austria and Israel respectively plotted on the overall ordinary events distributions of station 10 (Austria) and 375 (Israel) of the two land based datasets.

5.2 Parameters and quantiles

Identification of the distribution tails allowed us to derive the parameters describing them. Successively, by exploiting these results, extreme quantiles were computed.

The *shape* and *scale* parameters are fundamental quantities in the description of daily rainfall PDFs: while scale affects the distribution by stretching or shrinking it, the shape parameter changes its overall shape. These two deegrees of freedom interact by producing different consequences on ordinary and extreme events distribution.

Precisely, as visible in figure 5.3, if a reference probability distribution is defined, then, an increase (or overestimation) in the shape parameter would lead to a decrease (or underestimation) in the PDF tail, i.e. underestimation of extreme events, since it describes how quickly the negative exponential diminishes. Underestimation of the shape parameter, instead, would lead to an overestimation of the tail.

These differences affect the quantiles estimation also: in fact, if quantiles are derived by means of equation 2.20, high shape values would be related to greater quantiles underestimations for higher return periods and viceversa.

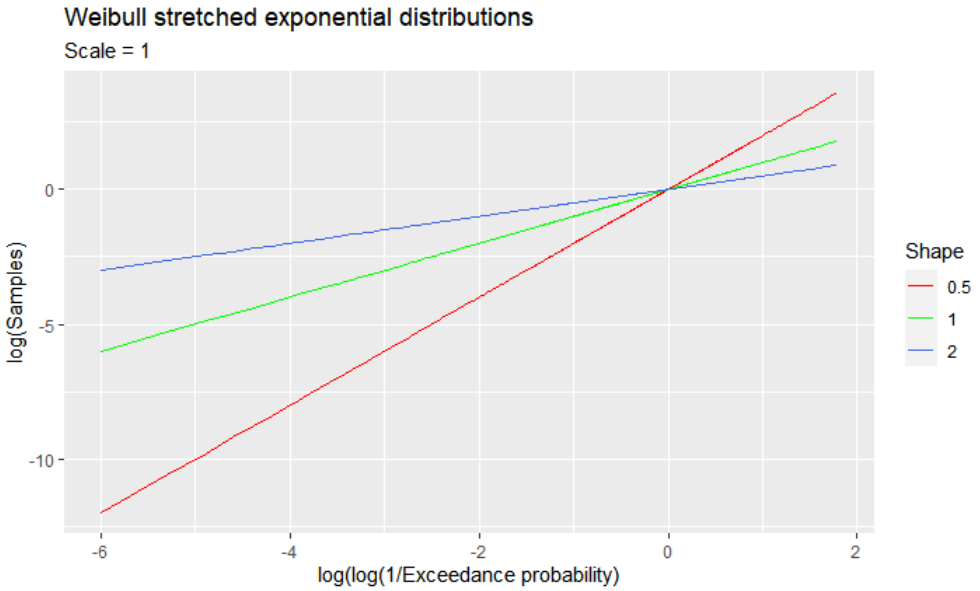

Figure 5.3: Weibull stretched exponential distributions in transformed coordinates with Scale parameter fixed to 1 and varying Shape parameter.

5.2.1 Parameters

Derived Mean number of yearly ordinary events (n), Shape and Scale parameters for both Austria and Israel were analyzed in scatterplots where land-based estimates are on the x axis and satellite-based ones were placed on the y axis so as to identify how and where the IMERG algorithm overestimated or underestimated them.

Mean number of yearly events

In figure 5.4, the n parameter scatterplots are shown, with the black line being x=y. In the Austria case, despite the fact that they cover a relatively small region, the stations present a high variability in the mean number of yearly ordinary events, with values ranging from little more than 150 to roughly 230. The satellite, instead, also due to the fact that just 8 pixels are considered for the 128 stations, shows very little dispersion with a mean value around 171 days. It is important to highlight that the IMERG product underestimates this parameter for most of the stations: this could be due to the measurement difference of the two types of instruments. In fact, rain gauges can collect water also below their minimum detectable threshold, then, when the volume of one side of the tipping bucket is full (which means that 0.11 mm of rain has been collected) the lever tips and the precipitation is recorded. Hence, if they collect precipitation in previous hours or day, it will appear as an ordinary 0.11 mm event not being observed by the satellite product. At the same time, since IMERG retrievals consider 8 pixels only, the fine scale variability of precipitation events is not reproduced as well as done by the rain gauges which report point values in a very dense network and this means that the estimate errors are more likely to be due to the satellite product.

The blue dot in the figure represents the long-recording *Bad Gleichenberg* station (not present in the Wegenernet Network), which reports precipitation data from 1948 and is located at $46.879°N$ and $15.907°E$. It has been used in preliminary evaluation of the datasets to spot differences between the new and highly sensitive network and the old long record.

In the Israel case, brown dots are related to the ARID climate stations, while green dots represent the MED ones. Here, a completely different situation was found: in fact, MED stations are characterized by both satellite overestimation and underestimation for events above the 1 mm selected threshold; ARID areas, instead, always show satellite overestimation. To explain the increased detection of events in these cases, two main aspects have to be taken into account: first, in Israel satellite pixels, the Mediterranean

and the Dead seas may be included, thus leading to grater noise in the detection of precipitation (moreover, the Dead sea is not masked as water surface by the retrieval algorithms in IMERG). Second, the climatic conditions are such that the precipitation events are typically due to convective processes, which could involve just one or few stations. However, when the satellite retrieval is applied, all the events recorded by the single stations in the considered satellite pixel (which gives areal estimates) result as summed up in the final number of events count. This last feature becomes more relevant for the ARID stations, since the few precipitation phenomena affecting these places are almost entirely convective [Sharon, 1972].

Shape and Scale

Looking at figures 5.5 (a) and 5.6 (a), it can be noticed that the Shape values, estimated as in section 4.2.1, are distinguished by an overall satellite overestimation for the Austrian dataset, thus leading to an underestimation effect on extremes with respect to land-based data. The Scale parameter is also characterized by overestimation, but, since this is related to an opposite effect on extremes, high quantiles estimates are expected to be less biased.

In the Israel case (figures 5.5 (b) and 5.6 (b)), both the Shape and Scale parameters estimates present underestimation for IMERG, which leads to overestimation and underestimation in extremes, respectively. Thus, high quantiles estimates should be less biased as for the Austrian network, even if the Scale estimates for the ARID area are generally higher for the satellite product.

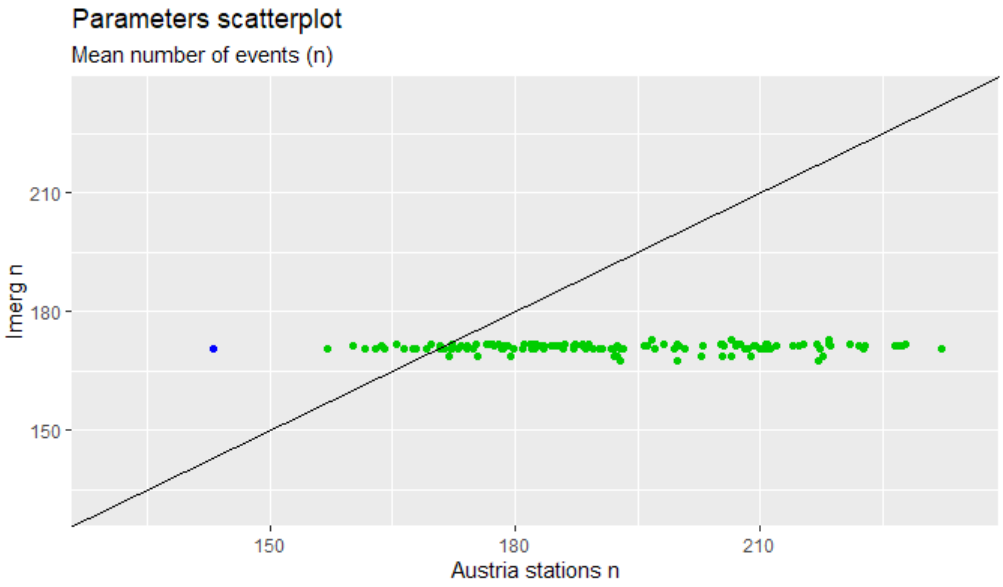

(a) Austria

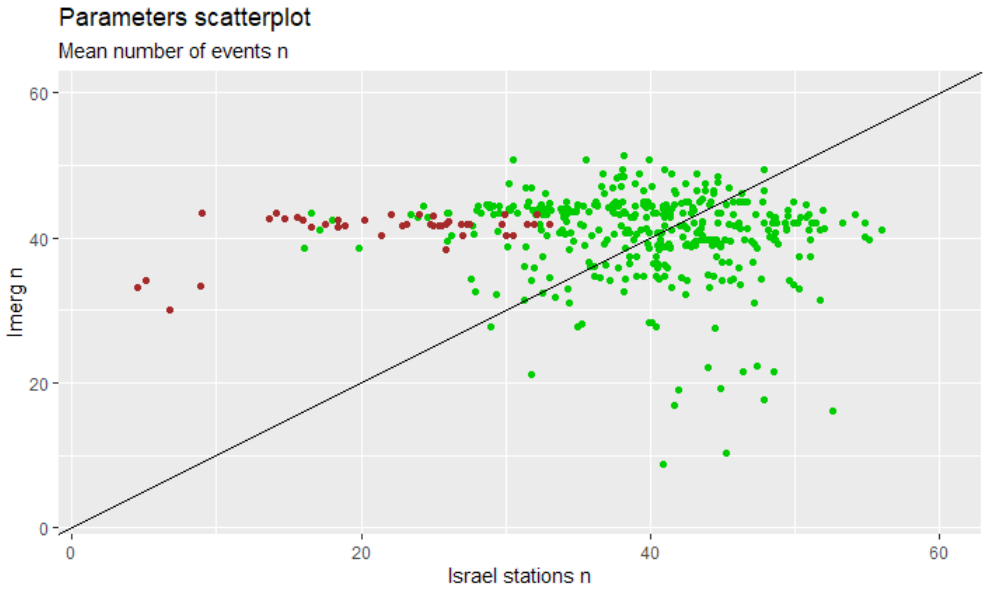

(b) Israel

Figure 5.4: Mean number of events (n) scatterplots. The blue dot represents the Bad Gleichenberg station for the Austria study area (figure a), while in Israel scatterplots (figure b) brown dots represent the estimates for the ARID stations and the green ones represent the estimates for the MED stations.

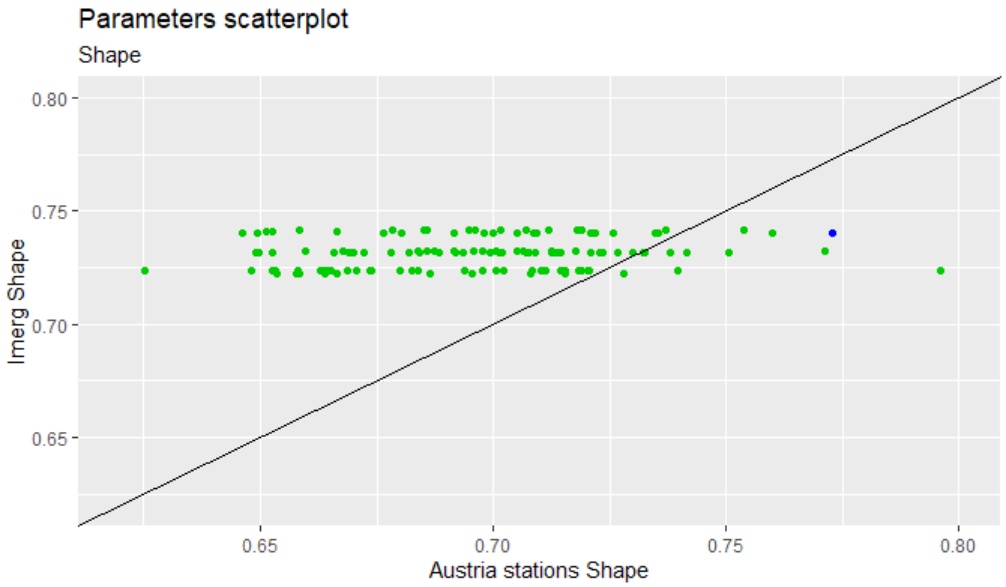

(a) Austria

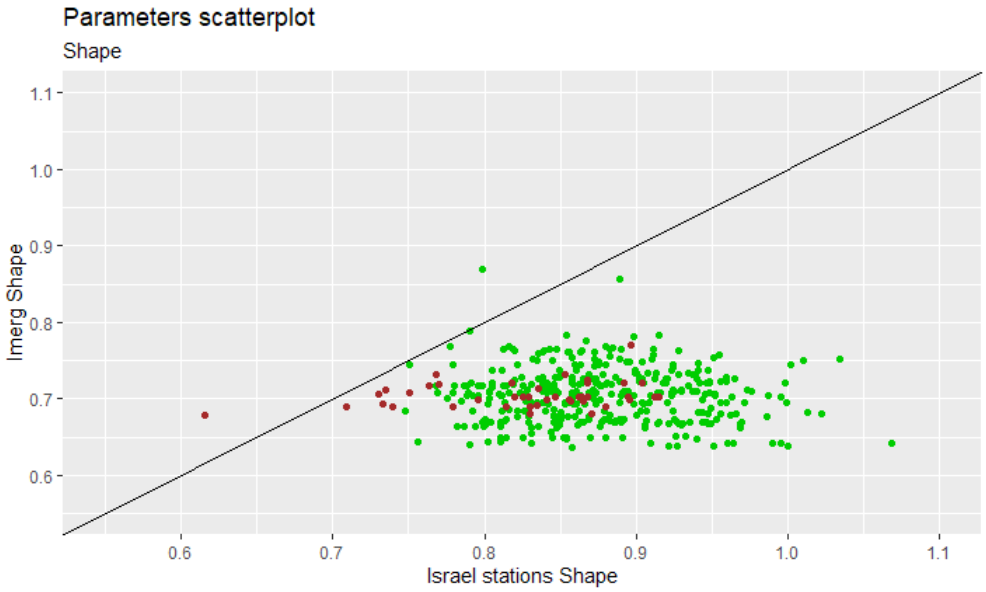

(b) Israel

Figure 5.5: Shape scatterplots. The blue dot represents the Bad Gleichenberg station for the Austria study area (figure a), while in Israel scatterplots (figure b) brown dots represent the estimates for the ARID stations and the green ones represent the estimates for the MED stations.

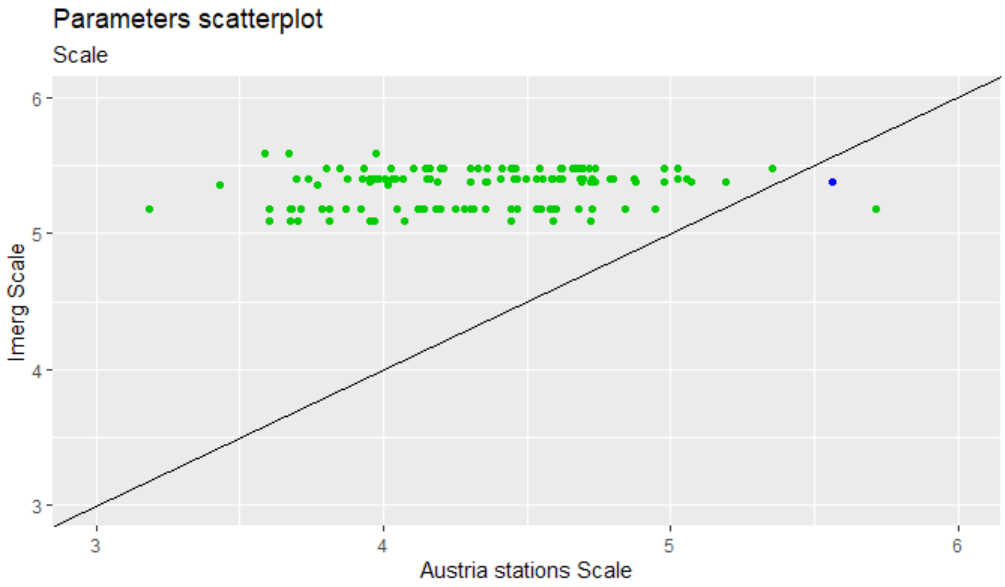

(a) Austria

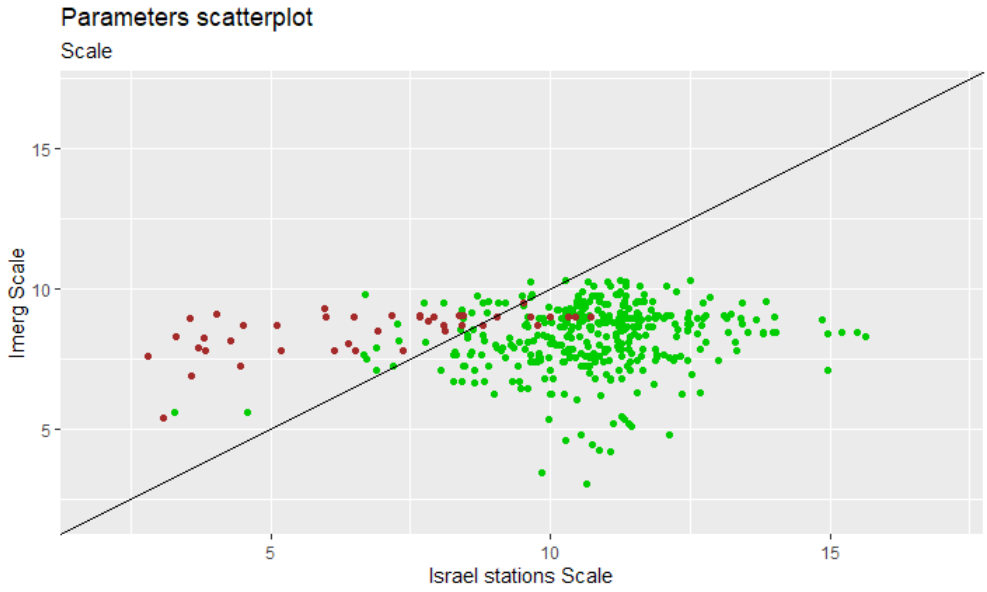

(b) Israel

Figure 5.6: Scale scatterplots. The blue dot represents the Bad Gleichenberg station for the Austria study area (figure a), while in Israel scatterplots (figure b) brown dots represent the estimates for the ARID stations and the green ones represent the estimates for the MED stations.

5.2.2 Quantiles

Quantiles estimation was done on the basis of parameters' results using eq. 2.20. Scatterplots of the IMERG versus stations' quantiles were obtained (figures 5.7, 5.8, 5.9, 5.10). In the Austria case study, a slight overall overestimation of the lowest studied quantiles (2, 5, 10 years return period) can be noticed, while for the highest return levels a better compensation is visible, due to the combination of overestimation for both the scale and shape parameters.

For the Israel case study, a different situation is detectable: in fact, a general overestimation affects all the computed quantiles. This could be due to the combination of two issues:

1 Shape underestimation is stronger than the Scale one

2 Shape weight in the inversion formula is bigger than the Scale one

Regarding point 1, as showed above, Israel shape estimates are characterized by an overall underestimation, with just two stations overestimated by IMERG, while, for the scale case, even if values have more dispersion, several cases (mainly ARID ones) exhibit larger satellite estimates with respect to rain gauges. Point 2 comes from the fact that, in the quantiles inversion formula, θ appears as a root index, while λ is just a multiplicative factor: this is corroborated by section 4.4 derivations, where it was shown that at the second order expansion the error in θ is the only not negligible term. This feature is better analyzed in the next paragraph where error propagation results are reported.

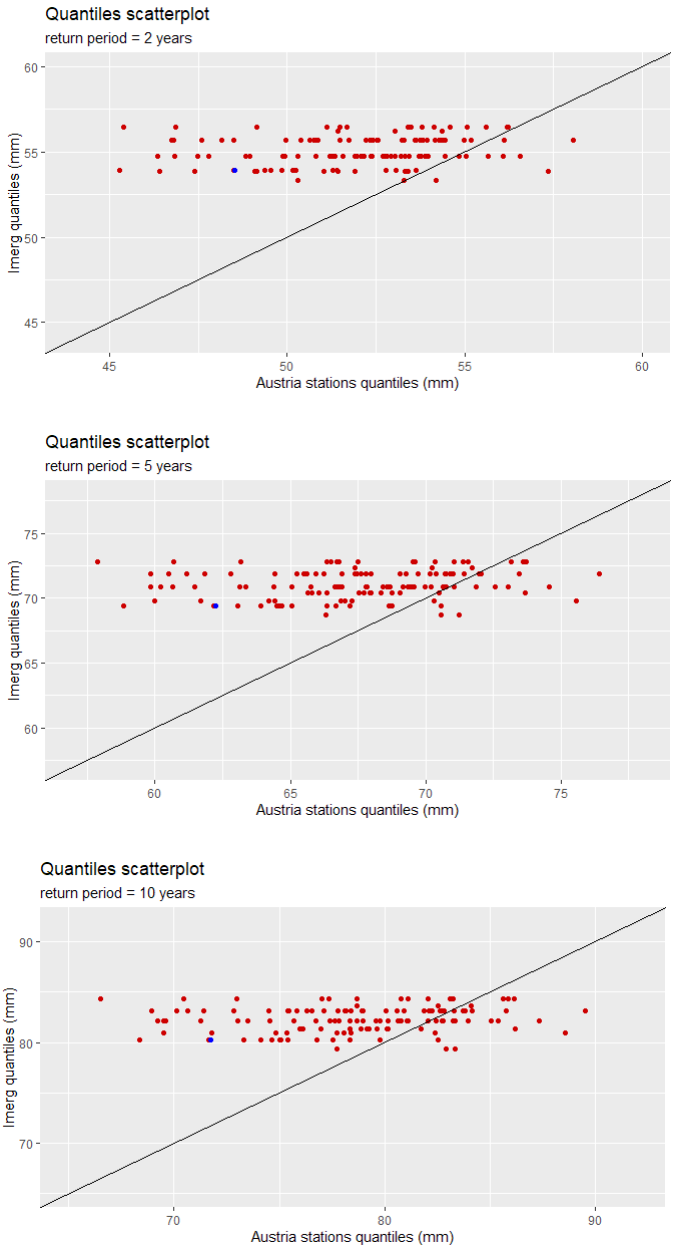

Figure 5.7: Austria derived quantiles: 2, 5, 10 years return period. Blue dot represents the Bad Gleichenberg station.

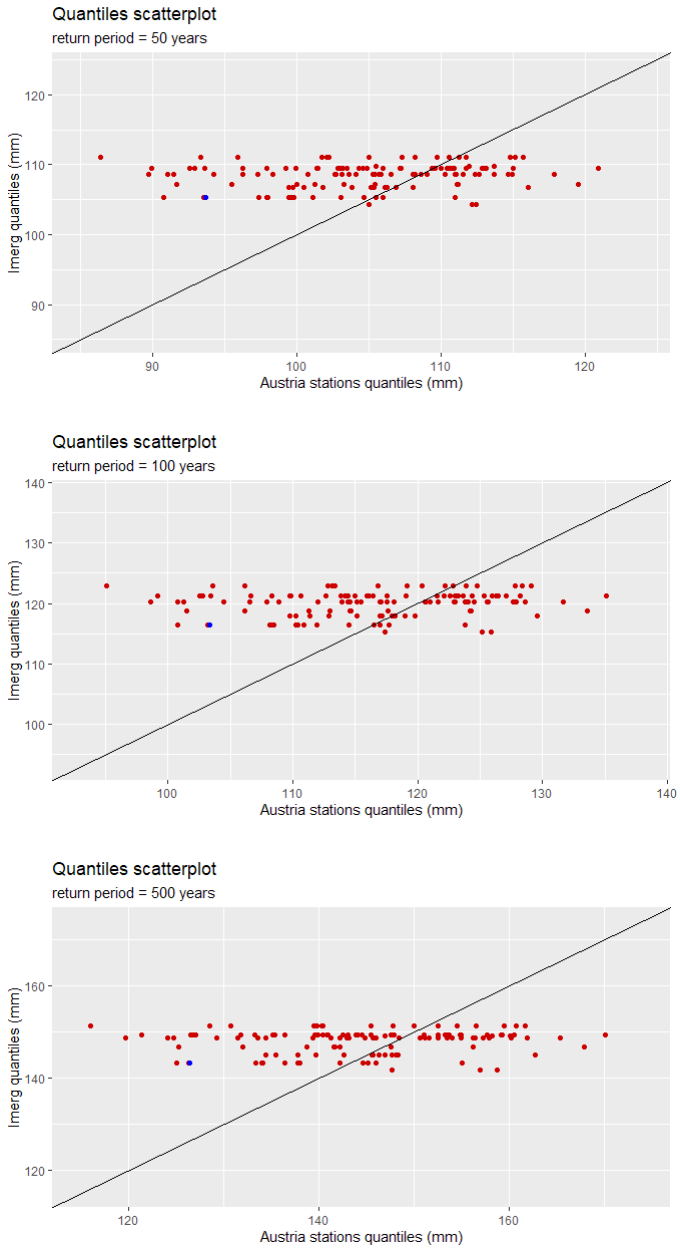

Figure 5.8: Austria derived quantiles: 50, 100, 500 years return period. Blue dot represents the Bad Gleichenberg station.

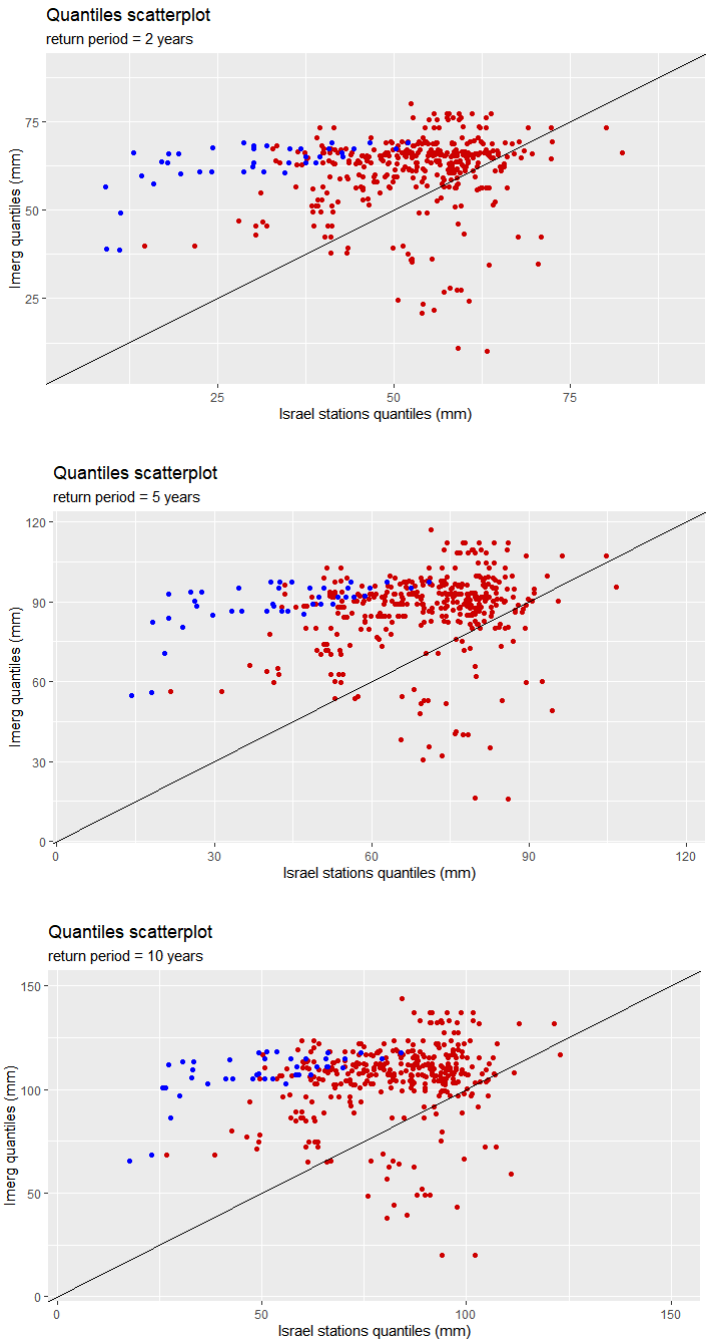

Figure 5.9: Israel derived quantiles: 2, 5, 10 years return period. Blue dots represent the ARID stations, red ones represent the MED stations.

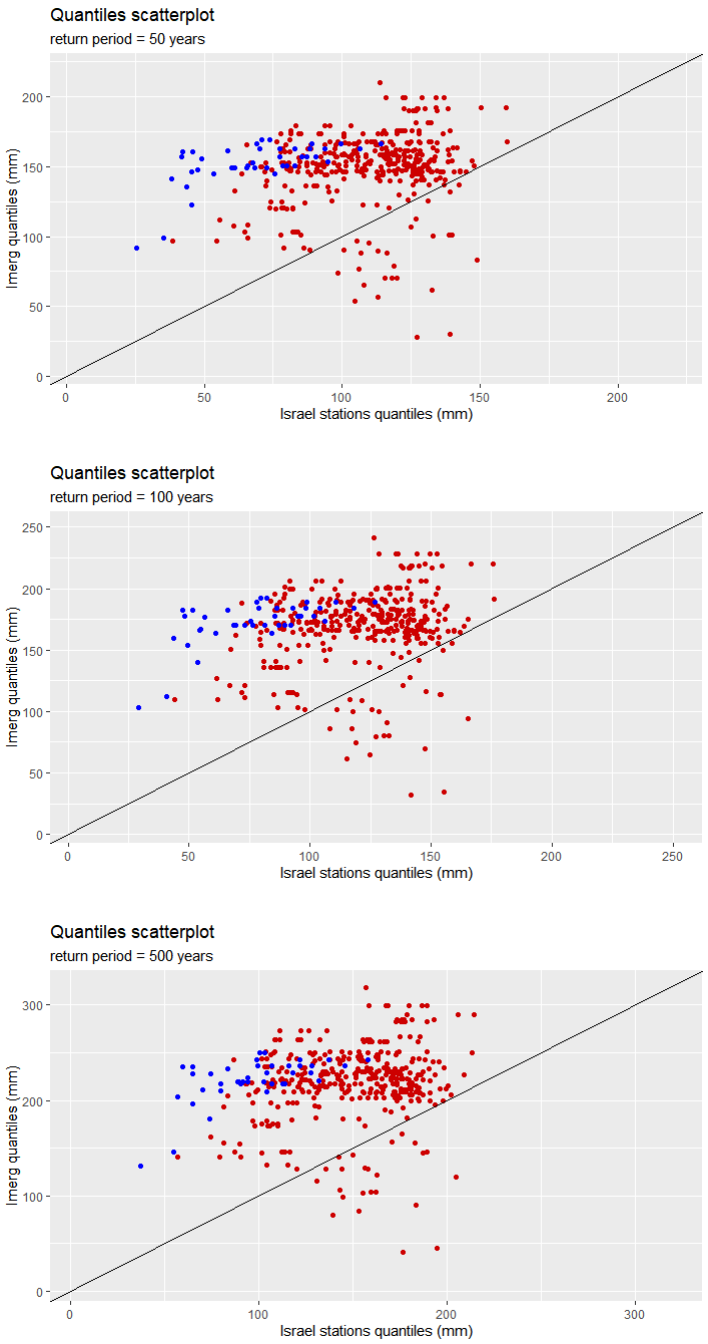

Figure 5.10: Israel derived quantiles: 50, 100, 500 years return period. Blue dots represent the ARID stations, red ones represent the MED stations.

5.3 Error propagation

This step consists of studying relationships between observed and estimated (computed by means of Taylor series expansion as in section 4.4) normalized quantiles' errors, so as to understand and quantify several parameters' estimation errors weight and reliability of the SMEV framework in parameters' and quantiles' estimation.

5.3.1 Austria

Figures 5.11 and 5.12 show scatterplots between normalized observed and estimated Austria errors. Differences between rain gauges and satellite are relatively small, in fact overestimations both for the two products with respect to each other never exceed 40%. Also, a good correlation between the two error types is visible even for low quantiles: in fact, all scatterplots' points lay near the x=y line, with better agreement for higher quantiles because approximations made in deriving the error equation are especially suited for extreme quantiles. Also, it can be noticed a slight tendency in overestimation for estimated (computed) errors, mostly for lower observed differences. Nevertheless, perfect agreement is never reached, since the section 4.4 equations are approximations truncated at the second order expansion.

5.3.2 Israel

In figures 5.13 and 5.14, scatterplots between normalized observed and estimated Israel errors are shown. In this case, differences between stations and satellite reach maximum values of nearly 500% for the 2 years return period quantiles. This bigger dispersion is due to the greater heterogeneity in stations' location and in climatic conditions; also, arid areas and sea surfaces increase noise in satellite retrievals.

A general underestimation for estimated errors is visible in case of higher observed differences (typical of ARID stations), but it constantly decreases for higher quantiles. In conclusion, a great agreement between estimated and observed quantile errors was found, which improves for higher return periods. Moreover, this improvement is way more visible in this case than in the Austrian one.

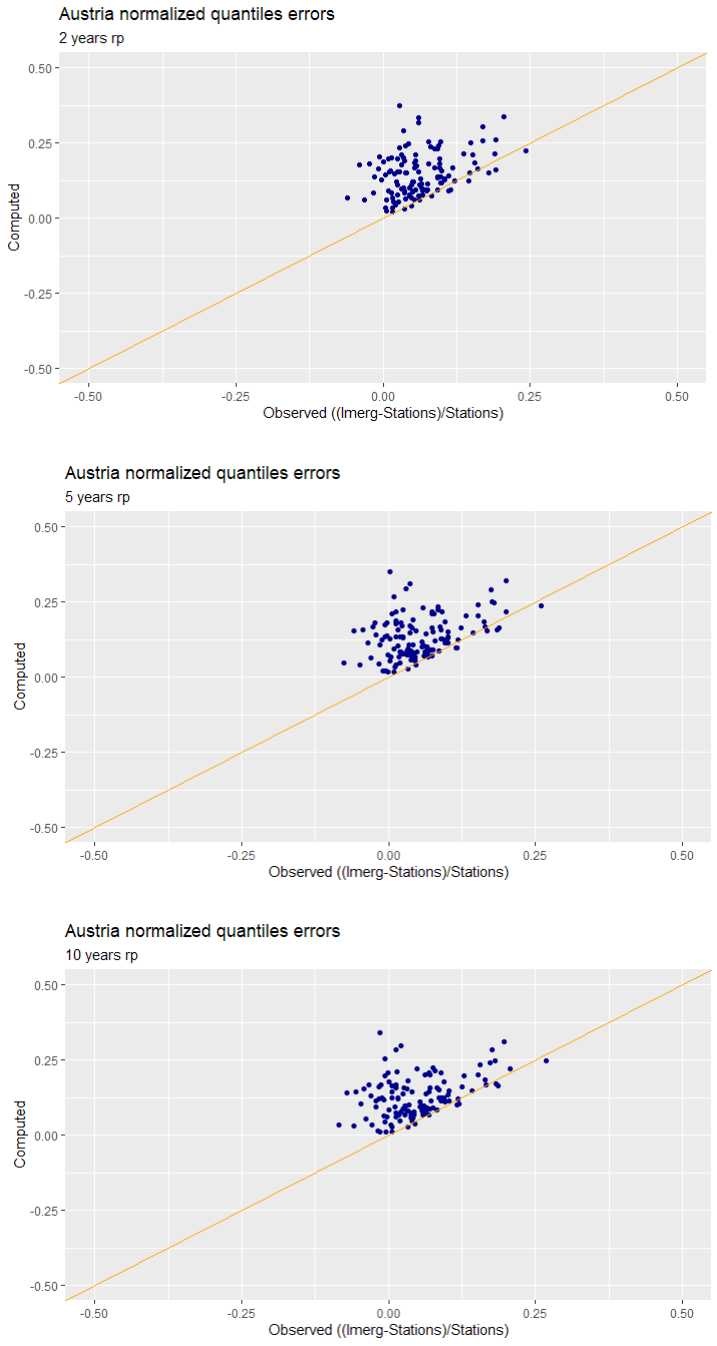

Figure 5.11: Austria error propagation: 2, 5, 10 years return period

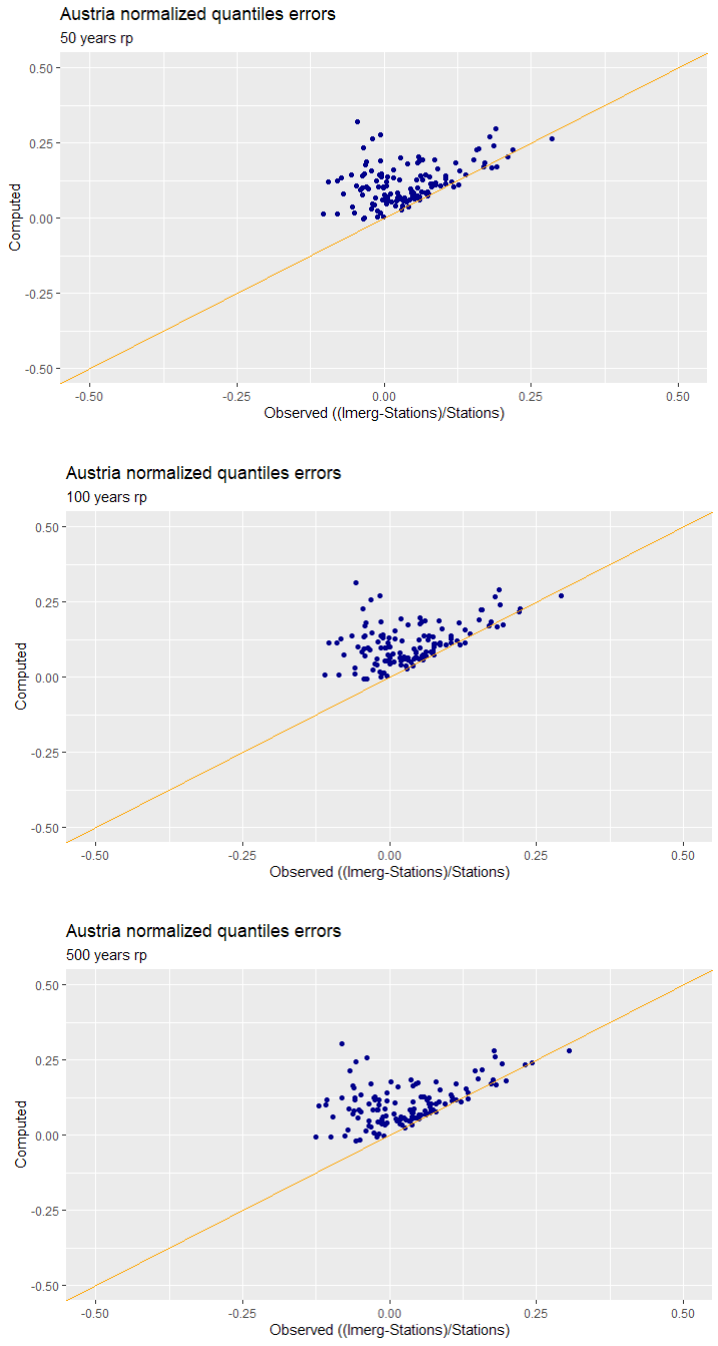

Figure 5.12: Austria error propagation: 50, 100, 500 years return period

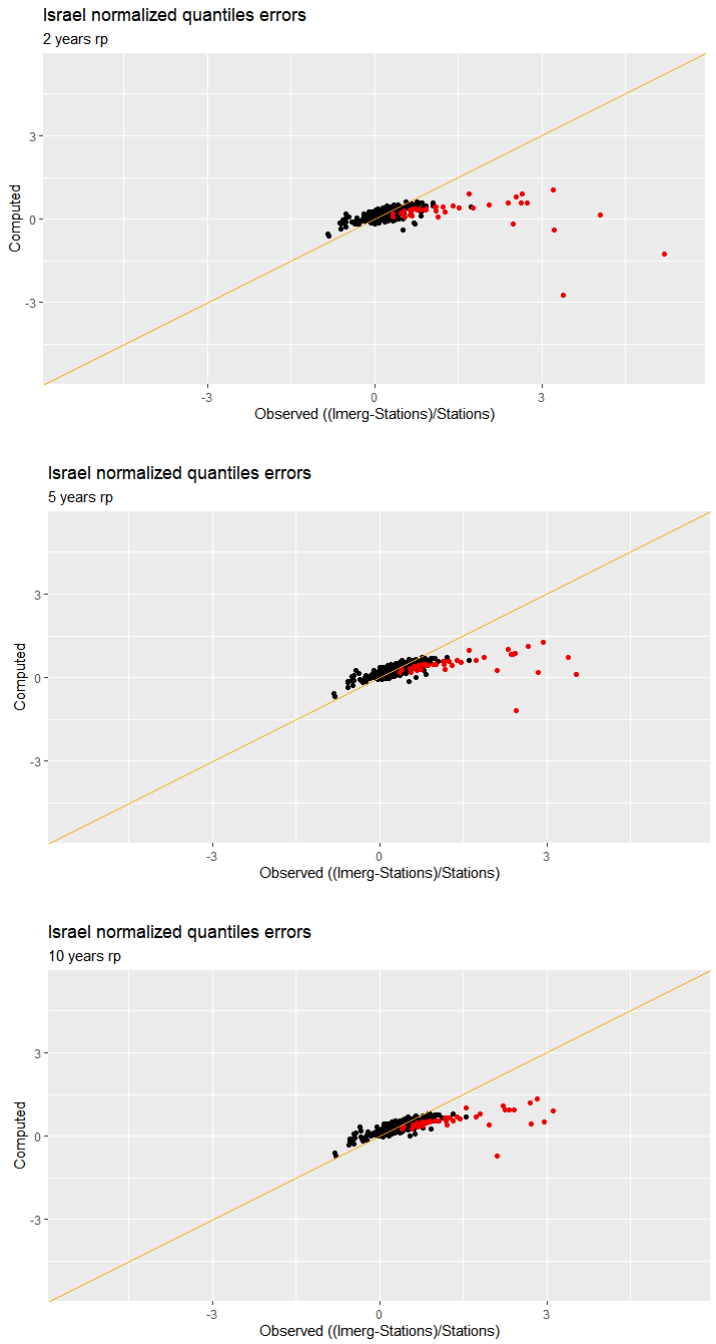

Figure 5.13: Israel error propagation: 2, 5, 10 years return period. Black dots represent MED stations, red dots represent ARID stations.

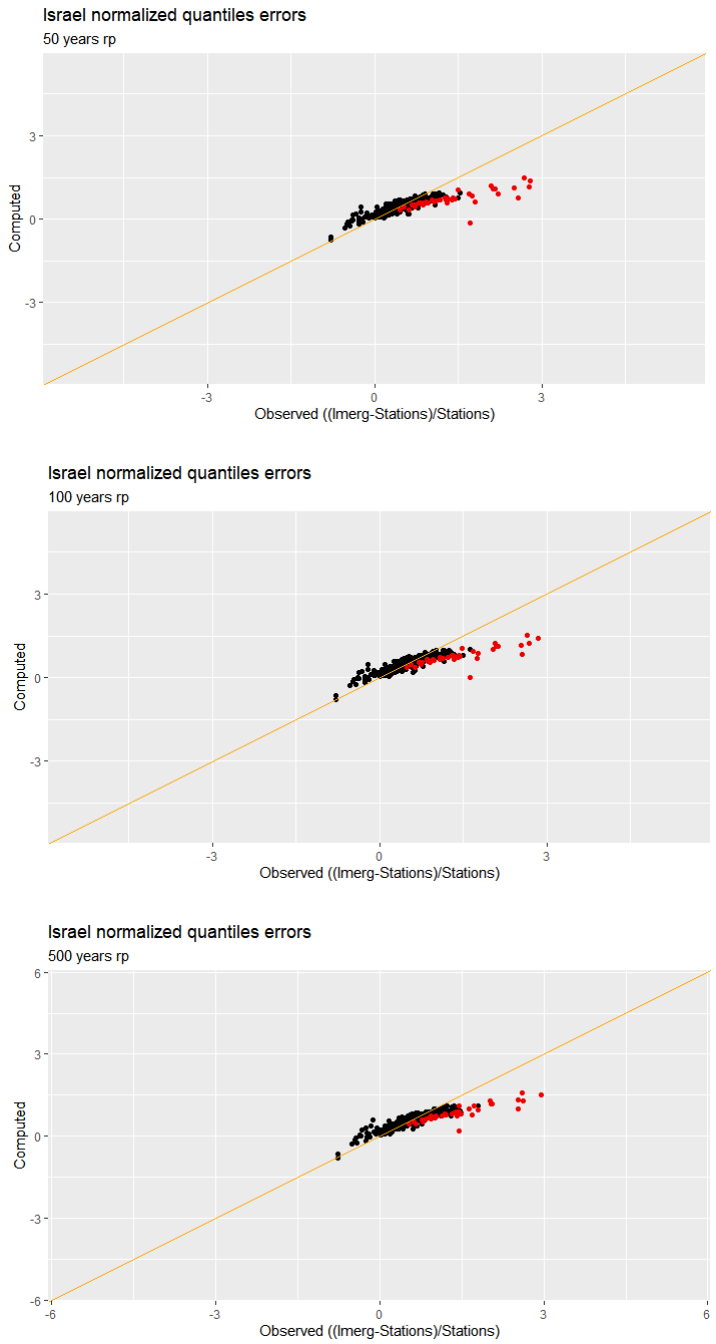

Figure 5.14: Israel error propagation: 50, 100, 500 years return period. Black dots represent MED stations, red dots represent ARID stations.

5.4 Moments-parameters correlation

Correlation between specific moments of the distribution errors, such as the *mean precipitation value* and its *standard deviation* above the selected left data portion (0.9 for Austria and 0.75 for Israel) and the parameters' errors was studied so as to see if derived quantities (the distribution parameters) could be related to the moments which can be obtained from prior knowledge of the satellite estimation errors.

The errors in this case are defined as bias, in particular as the ratio between IMERG and stations estimates. The blue and yellow lines in the following figures represent the linear fit based on the plotted dots, while the green shading represents the 90% confidence interval.

5.4.1 Austria

Figures 5.15 and 5.16 show Austrian correlations for scale and shape parameters respectively.

It can be noticed that a modest correlation is identifiable between scale and mean precipitation value errors (fig. 5.15 (a)), where the R^2 value is equal to 0.450, even if dispersion is not negligible, mostly for higher bias. Standard deviation (fig. 5.15 (b)), instead, doesn't show signs of an actual correlation: in fact, the R^2 term is nearly 0.

Shape errors are characterized by a completely different tendency, in fact some correlation is visible between them and standard deviation biases (fig. 5.16 (b)) with an R^2 value of 0.372. Mean precipitation value errors (fig. 5.16 (a)), instead, don't show interdependence: R^2 is nearly 0 and the dispersion is high.

5.4.2 Israel

In this case, ARID stations have been highlighted with red dots to distinguish them from the MED ones in figures 5.17 and 5.18.

The greater number of stations and the better match between Israel ordinary events tail and the Weibull distribution reduced the dispersion in fit estimates for the scale errors: as shown in fig. 5.17 (a), a very high correlation was found for mean precipitation value errors with $R^2 = 0.891$. ARID stations in this case increase the degree of correlation since they are distributed close to the linear fit, even if characterized by greater bias values. Standard deviation also shows a slight correlation with the scale parameter (fig. 5.17 (b)), in fact $R^2 = 0.486$. As opposed to the mean precipitation value errors,

ARID stations are characterized by high dispersion, due to the greater noise of satellite retrievals for these areas.

Israel shape errors don't show sign of noticeable correlations with the Mean precipitation value differences (5.17 (a)). Standard deviation errors (5.17 (b)) appear as uncorrelated if linear fit is done on all the stations, but if the ARID stations are filtered out, the R^2 value increases considerably to 0.357 as visible in figure 5.19.

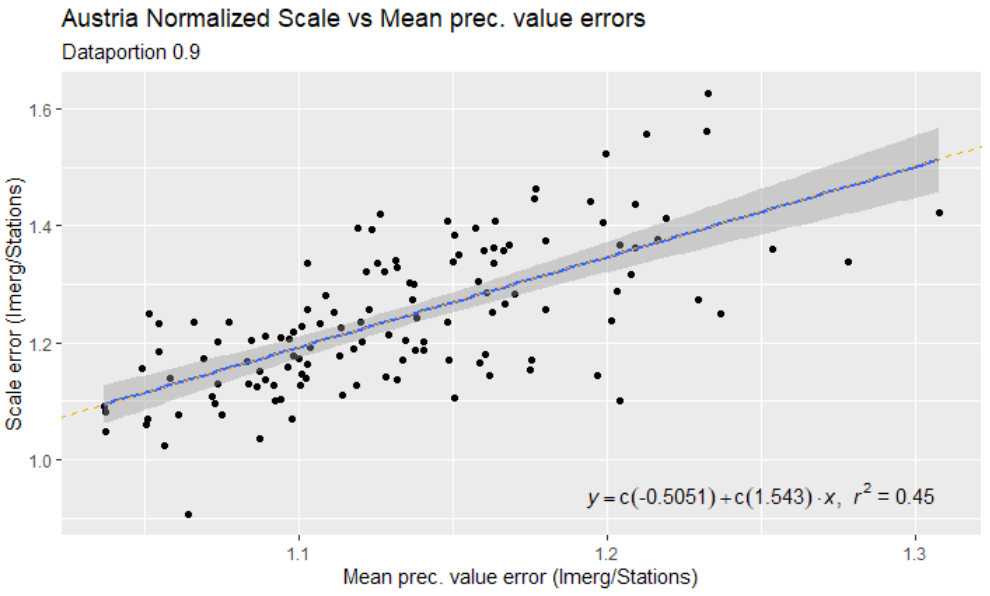

(a)

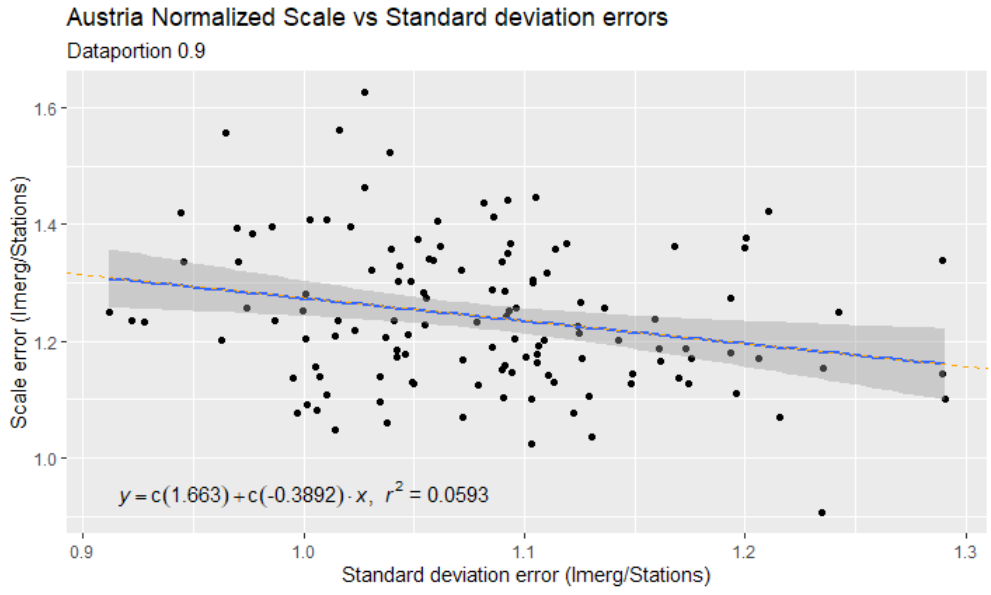

(b)

Figure 5.15: (a). Austria Scale error vs. Mean precipitation error (b). Austria Scale error vs. Mean precipitation standard deviation error

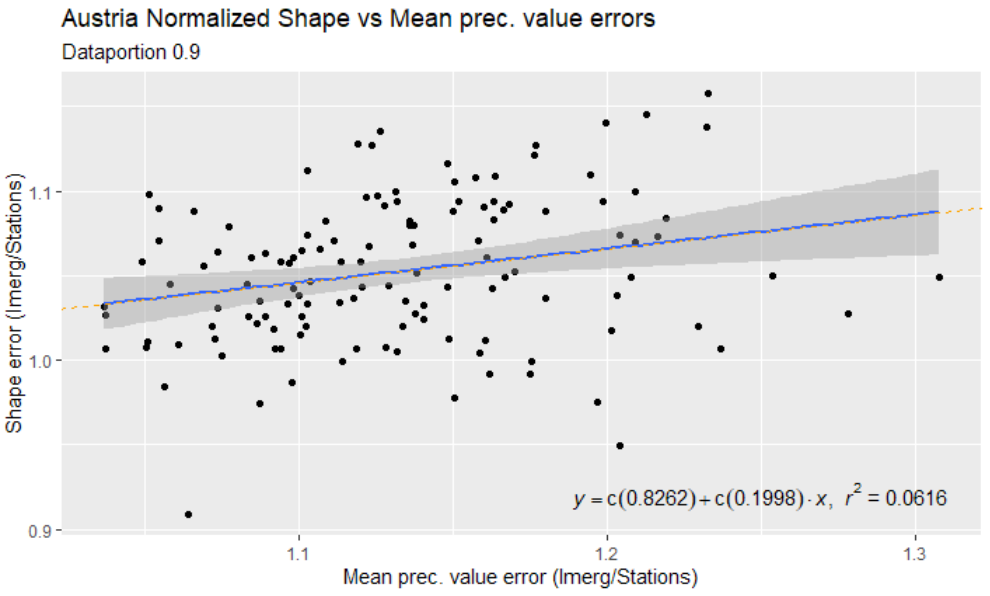

(a)

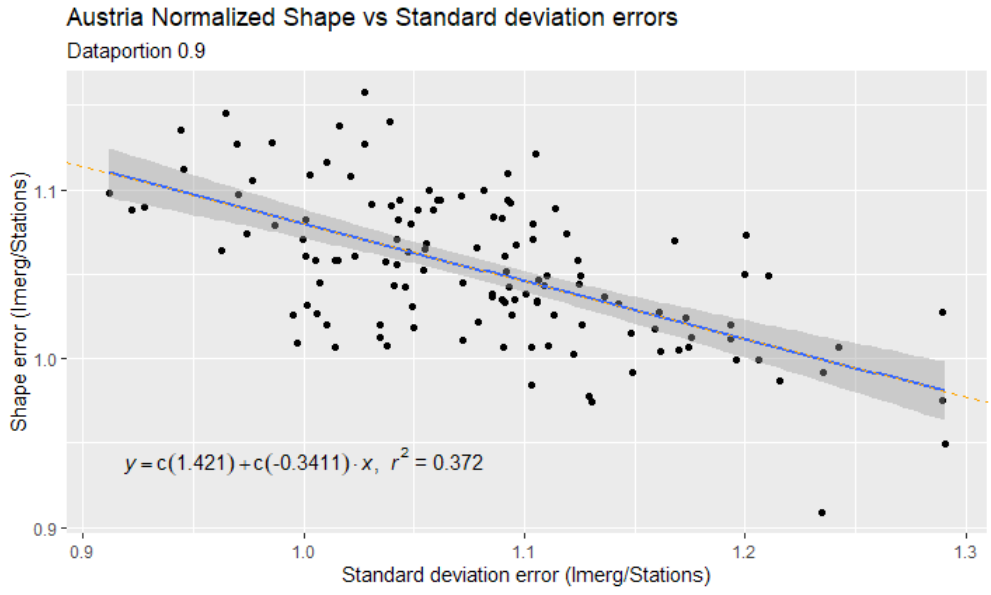

(b)

Figure 5.16: (a). Austria Shape error vs. Mean precipitation error (b). Austria Shape error vs. Mean precipitation standard deviation error

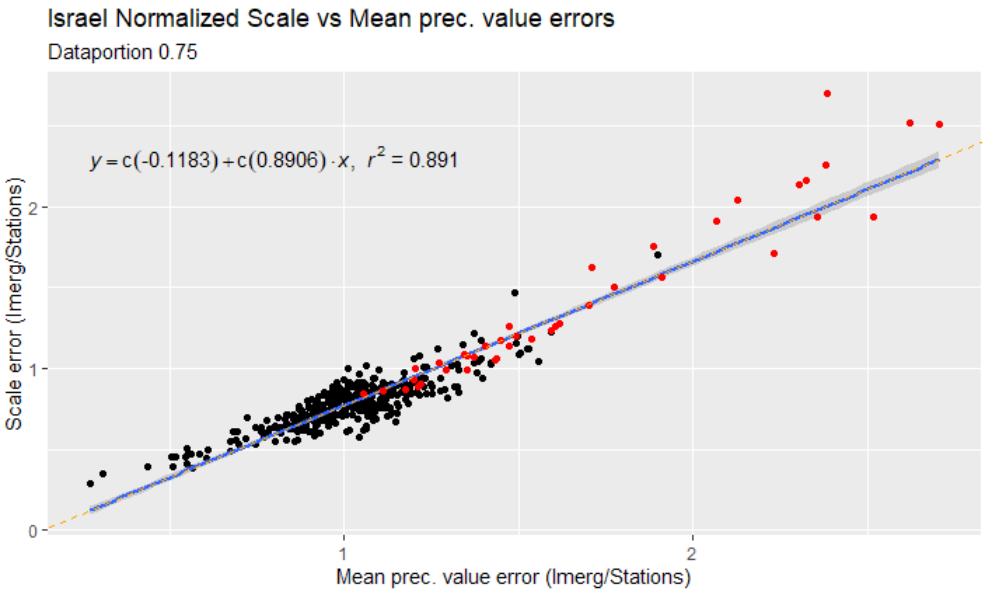

(a)

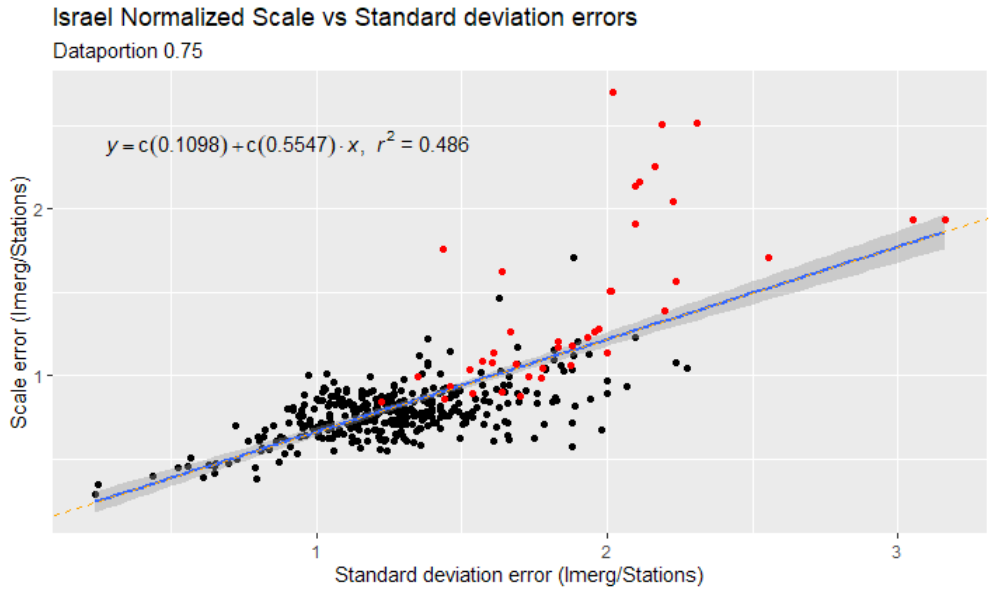

(b)

Figure 5.17: (a). Israel Scale error vs. Mean precipitation error (b). Israel Scale error vs. Mean precipitation standard deviation error

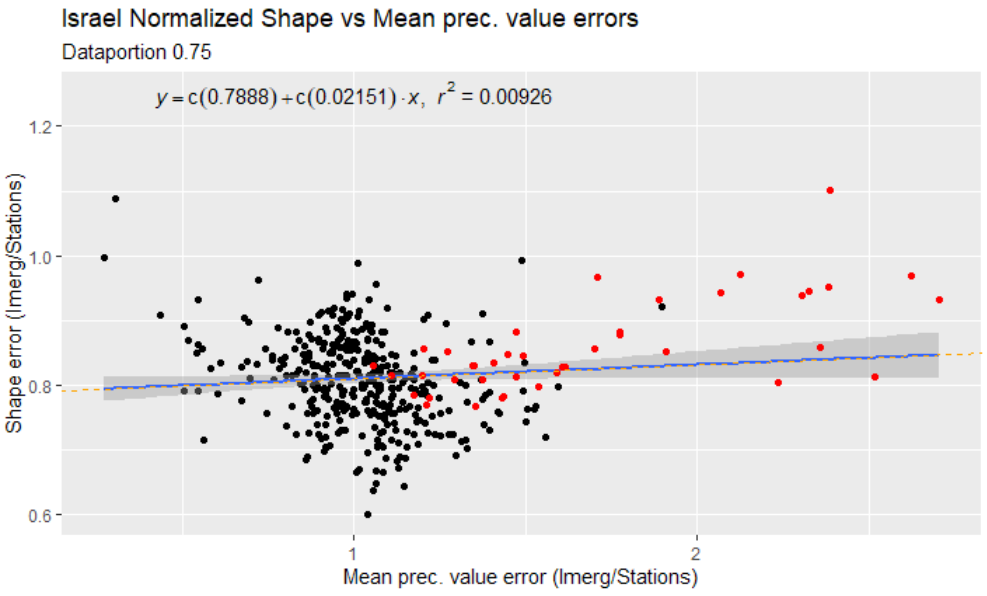

(a)

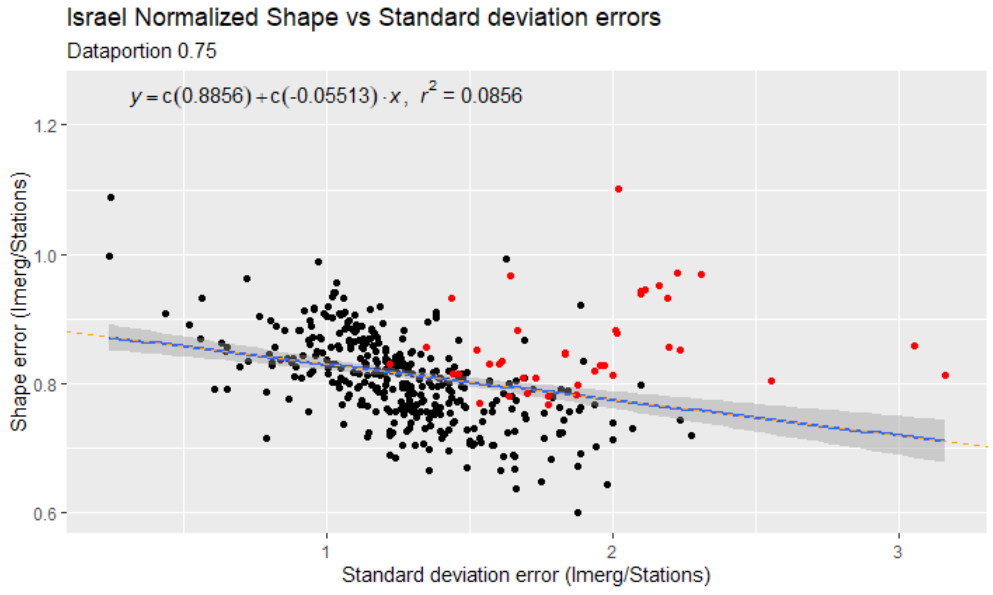

(b)

Figure 5.18: (a). Israel Shape error vs. Mean precipitation error (b). Israel Shape error vs. Mean precipitation standard deviation error

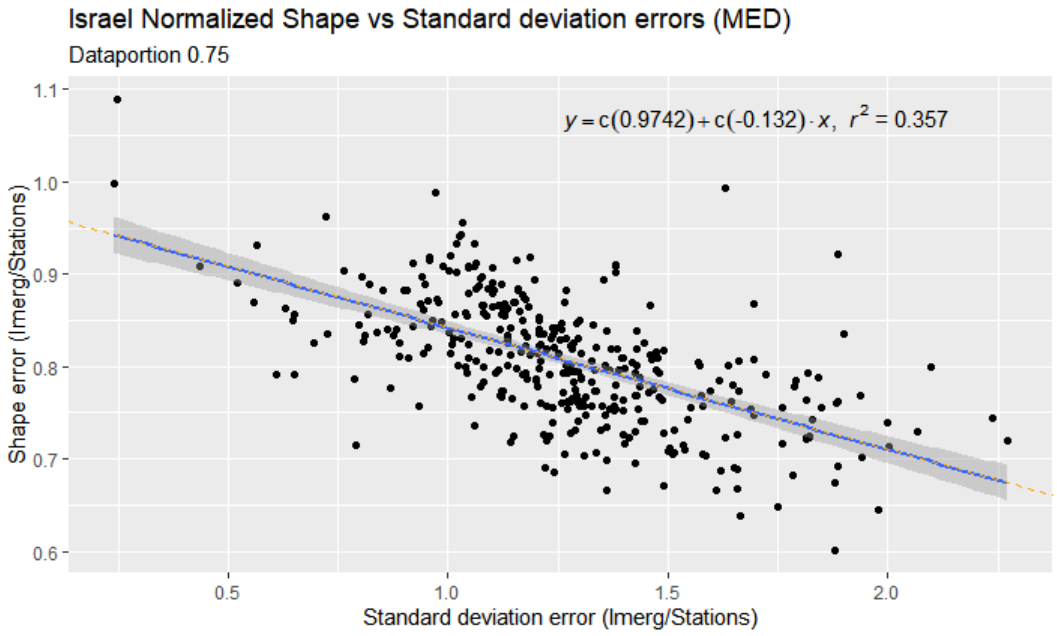

Figure 5.19: Israel Shape error vs. Mean precipitation standard deviation error for MED stations only.

Chapter 6

Summary and Conclusions

In this work, satellite (IMERG V06) and land based precipitation data have been studied and analyzed with the overarching objective of improving the estimation of high return period quantiles from satellite observations. These extreme precipitation events are of main concern in several fields, such as hydrological design, insurance and reinsurance businesses, natural hazard risk estimation and management and many other applications.

Satellite data are of fundamental relevance in the process of precipitation frequency analysis because of the scarce land coverage of rain gauges: their uneven distribution doesn't allow to obtain enough information on the most remote parts of the globe and on the sea surface.

Since very few studies on assessing differences between land and satellite based precipitation measurements have been done so far and error correlation between derived quantiles for the two types of instruments has not been well described yet, in this thesis several steps in the direction of closing these gaps were made.

Study areas with very different characteristics were selected: a portion of south-eastern Austria and the whole territory of Israel. This allowed to identify three main climatic zones: 1 for Austria, which belongs to the warm-summer humid continental climate Dfb, and 2 for Israel, which have been labelled as "Mediterranean" (or MED, for Csa zones) and "Arid" (or ARID, for BSh and BWh zones).

In the first place, data quality was checked and ordinary events, i.e. daily precipitation data defined as realization of independent stochastic variables, were defined by identifying the right daily precipitation threshold for both the study areas.

Then, a preliminary test, based on the SMEV statistical framework, that is a simplified version of the Metastatistical Extreme Value framework, was applied to the land based data, considered as the reference, so as to iden-

tify the ones which belong to the precipitation probability distribution tail. Afterwards, distribution parameters and high return period quantiles were derived for both satellite and stations data regarding all the study areas. Then, differences in these derivations between the two instruments were analyzed and correlated so as to understand gaps and errors and how to adjust them.

The results achieved in this work can be summarized as follows:

- The daily precipitation threshold for the Austrian data was set to 0.1 mm, because the difference in daily precipitation estimation is very slight for the rain gauge and satellite products. In the case of Israel, due to the presence of the ARID area, whose station data are characterized by a very high dispersion, and of the Mediterranean and Dead sea in the satellite pixels, noise is way more emphasized, thus leading to pronounced differences in satellite daily event estimates with respect to rain gauges ones. This led to choosing 1 mm as the threshold value, since starting from this quantity the overestimation for satellite retrievals is almost null.

- Distribution tail identification, carried out by comparing several portions of the stations' ordinary events to Weibull stretched exponential distributions, led to the choice of selecting the highest 10% and 25% ordinary events for Austria and Israel, respectively, as the values representing the tail. In fact, Weibull distributions, obtained from the parameters estimated on the basis of the tail events so defined, fit very well these portions of the probability distributions, while they increasingly deviate while approaching lower values. For the Israel case study, correspondence starts at lower non exceedance probability values since precipitation events characterizing this area are mostly convective. They better adapt to Weibull distributions, also because of the fact that they are more likely to happen within one day and thus to be independent.

- Parameter estimation led to different results for the analyzed areas. The mean number of yearly ordinary events shows a high variability roughly ranging from 150 to 230 days for Austrian stations, despite the fact that the network covers a very small region around the city of Feldbach. The IMERG product underestimates it for most of the rain gauges: this could be due to the fact that IMERG retrievals consider 8 pixels only, so the fine scale variability of precipitation events is not reproduced as well as done by the rain gauges which report point values

in a very dense network. Furthermore, the tipping buckets of the stations collect rain below their detectable threshold, but they tip when the volume of each of them is full (thus precipitation under the threshold happened in previous day is recorded as daily values in the next ones), that is when 0.11 mm of water has been gathered; meanwhile satellite products just capture radiation corresponding to precipitation signals greater than or equal to their detection threshold, so they end up in recording less daily events.

- As to Israel's mean number of yearly ordinary events analysis, ARID and MED stations were separated: this allowed to notice that while the ARID rain gauges are characterized by systematic overestimation of the ordinary events above the 1 mm threshold, the MED stations show overall compensation between overestimation and underestimation of this parameter. The overestimates could be due to two main issues: firstly, satellite pixels include sea surface from the Mediterranen and Dead seas, whose noise leads to an increase in detection of precipitation events; secondly, the climatic zones are such that convective precipitation is way more likely to happen with respect to the stratiform type, so when events affect individual stations, satellite product just sums up all the events happened in one pixel which may include several stations.

- Austria shape and scale parameters estimates are characterized by overall satellite overestimation. Since they have an opposite effect on quantiles' derivation (scale is a multiplicative factor, shape is the index of a logarithm's root), they lead to a general compensation when these are computed, which becomes more relevant for higher return periods. This could be due to the fact that shape overestimation is related to very high extremes underestimation, while if scale is overestimated, extremes are overestimated like all the other distribution values. For the Israel case study, shape parameter values showed IMERG underestimation for almost all the stations. Scale estimates, instead, are characterized by sharp overestimation for ARID stations and overall underestimation for MED stations. This led to a general overestimation of the quantiles, whose dispersion decreases for higher return periods, because of the facts that shape overall underestimation is stronger than the scale one and that this parameter's weight in the inversion formula for retrieving quantiles is bigger than the scale one.

- Observed errors, defined as normalized differences between IMERG and rain gauges derived quantiles, were analyzed and compared to esti-

mated errors obtained from the second order Taylor series expansion. Even if over and under-estimations between the two products are larger for Israel, both the study areas showed a considerable agreement between observed and estimated errors, with increasing match for higher quantiles, due to the fact that approximations, which are more valid for higher quantiles, were made in deriving second order error propagation equations. Also, Austrian errors are characterized by a slight Taylor expansion overestimation, especially for low differences, while, for Israel, a tendency in underestimation for higher errors was found.

- Correlation between parameters and moments of the distribution errors (IMERG/stations) showed that the scale errors are strongly correlated with the mean precipitation value above the selected left data portion threshold for both the study areas. At the same time, the standard deviation error of the mean precipitation value is characterized by a slight anti-correlation with the shape parameter errors for both the areas; but for Israel this relation becomes valuable if MED stations are considered only, while it decreases considerably if ARID stations are added in the fitting.

6.1 Outlook

These results will possibly help in improving and adjusting satellite retrievals over regions of the globe poorly covered by rain gauges and characterized by climatic conditions analogous to those analyzed in this work. The moments-parameters error correlation allowed us to understand which are the connections between derived quantities and those available by prior knowledge of the probability distribution of the ordinary events, so these results can be applied to other remote or scarcely sampled areas such as oceans, deserts and rain forests.

Future applications will hopefully focus on applying the methods exploited in this thesis to other regions with climatic conditions different from the ones here analyzed, possibly with dense and reliable rain gauges networks which can be used as reference for preliminary evaluation. Another future implementation should be based on the analysis of areal means of the station data: in fact, satellite pixels usually include several stations, so that analysis of averaged land based values could give estimates closer to the satellite retrievals.

Glossary

ARID Israel stations in the BSh and BWh climate zones.

ECDF Empirical Cumulative Distribution function.

EVT Extreme Value Theory.

GEV Generalized Extreme Value distribution.

GPM Global Precipitation Measurement mission.

IMERG Integrated Multi-SatellitE Retrievals algorithm for the GPM mission.

MED Israel stations in the Csa climate zone.

MEV Metastatistical Extreme Value framework.

PDF Probability Density Function.

RP Return Period.

SMEV Simplified Metastatistical Extreme Value framework.

TRMM Tropical Rainfall Measuring Mission.

References

Abarbanel, H., Koonin, S., Levine, H., MacDonald, G., Rothaus, O. (1992). Statistics of Extreme Events with Application to Climate. *JASON*, JSR-90-30S

Becker, A., Finger, P., Meyer-Christoffer, A., Rudolf, B., Schamm, K., Schneider, U., Ziese, M. (2013). A description of the global land-surface precipitation data products of the Global Precipitation Climatology Centre with sample applications including centennial (trend) analysis from 1901–present. *Earth System Science Data*, 5, 71-99

Berg, P., Moseley, C., Haerter, J.O. (2013). Strong increase in convective precipitation in response to higher temperatures. *Nature Geoscience Letters*, 6, 181-185

Brunetti, M. Personal notes of "Climatology" class a.y. 2019/2020.

Chow, V.T, Maidment, D.R., Mays, L.W. (1988). Applied Hydrology. *McGraw-Hill*

Coles, S. (2001). An introduction to statistical modeling of extreme values. *Springer*

Cook, N., Harris, N., (2004). Exact and general FT1 penultimate distributions of extreme wind speeds drawn from tail-equivalent Weibull parents. *Structural Safety*, 26, 391-420

Fischer, E.M., Knutti, R. (2016). Observed heavy precipitation increase confirms theory and early models. *Nature Climate Change*, 6, 986-991

Fischer, R.A., Tippet, L.H.C. (1928). Limiting forms of the frequency distribution of the largest or smallest member of a sample. *Proceedings of the Cambridge Philosophical Society*, 24, 180-190

Fuchsberger, J., Kirchengast, G., Bichler, C., Leuprecht, A., Kabas, T. (2021). WegenerNet climate station network Level 2 data version 7.1 (2007–2020). *Wegener Center for Climate and Global Change, University of Graz, Austria*, https://wegenernet.org/portal/v7.1/2021/1

Gado, T.A., Hsu, K., Sorooshian, S. (2017). Rainfall frequency analysis for ungauged sites using satellite precipitation products. *Journal of Hydrology*, 554, 646-655

Gnedenko, B.V. (1943). Sur la distribution limite du terme maximum d'une serie aleatoire. *Annals of Mathematics*, 44, 423-453

Gumbel, E.J. (1958). Statistics of Extremes. *Columbia University Press*

Hong, Y., Hsu, K.L., Sorooshian, S., Gao, X. (2004). Precipitation estimation from remotely sensed imagery using an artificial neural network cloud classification system. *Journal of Applied Meteorology*, 43, 1834–1853

Hor, C., Watson, S., Infield, D., Majithia, S. (2008). Assessing load forecast uncertainty using extreme value theory. *16th PSCC, Glasgow, July 14-18, 2008*

Hou, A.Y., Kakar, R.K., Neeck, S., Azarbarzin, A.A., Kummerow, C.D., Kojima, M., Oki, R., Nakamura, K., Iguchi, T. (2014). The global precipitation measurement mission. *Bulletin of the American Meteorological Society*, 95, 701-722

Hu, L., Nikolopoulos, E.I., Marra, F., Morin, E., Marani, M., Anagnostou, E.N. (2018). Evaluation of MEVD-based precipitation frequency analyses from quasiglobal precipitation datasets against dense rain gauge networks. *Journal of Hydrology*, 590, 125564

Huffman, G.J., Bolvin, D.T., Braithwaite, D., Hsu, K., Joyce, R., Xie, P., Yoo, S.H. (2015). NASA global precipitation measurement (GPM) integrated multi-satellite retrievals for GPM (IMERG). *Algorithm Theoretical Basis Document (ATBD) Version 4*, 26

Huffman, G.J., Bolvin, D.T., Nelkin, E.J., Wolff, D.B., Adler, R.F., Gu, G., Hong, Y., Bowman, K.P., Stocker, E.F. (2007). The TRMM multisatellite precipitation analysis (TMPA): quasi-global, multiyear, combined-sensor precipitation estimates at fine scales. *Journal of Hydrometeorology*, 8, 38–55

Joyce, R.J., Xie, P. (2011). Kalman filter–based CMORPH. *Journal of Hydrometeorology*, 12, 1547–1563

Katz, R., Parlange, M., Naveau, P. (2002). Statistics of extremes in hydrology. *Advances in water resources*, 25, 1287-1304

Kidd, K., Becker, A., Huffman, G.J., Muller, C.L., Joe, P., Skofronick-Jackson,G., Kirschbaum, D.B. (2017). So, how much of the Earth's surface is covered by rain gauges? *Bulletin of the American Meteorological Society*, 98(1), 69–78

Kidd, C., Levizzani, V. (2011). Status of satellite precipitation retrievals. *Hydrology and Earth System Sciences*, 15, 1109-1116

Köppen, W., Geiger, R. (1936). Das geographisca System der Klimate. *Handbuch der Klimatologie*

Koutsoyiannis, D. (2004). Statistics of extreme and estimation of extreme rainfall: I. Theoretical investigation. *Hydrological Sciencies Journal*, 49, 575-590

Marani, M., Ignaccolo, M. (2015). A Metastatistical approach to rainfall extremes. *Advances in Water Resources*, 79, 121-126

Marra, F., Armon, M., Adam, O., Zoccatelli, D., Gazal, O., Garfinkel, C., Rostkier-Edelstein, D., Dayan, U., Enzel, Y., Morin, E. (2021). Toward Narrowing Uncertainty in Future Projections of Local Extreme Precipitation *Geophysical Research Letters*, 48

Marra, F., Borga, M., Morin, E. (2020). A unified Framework for Extreme Subdaily Precipitation Frequency Analyses Based on Ordinary Events. *Geophysical Research Letters*, 49

Marra, F., Nikolopoulos, E.I., Anagnostou E.N., Bárdossy, A., Morin, E. (2019). Precipitation frequency analysis from remotely sensed datasets: A focused review *Journal of Hydrology*, 574, 699-705

Marra, F., Nikolopoulos, E.I., Anagnostou, E.N., Morin, E. (2018). Metastatistical Extreme Value analysis of hourly rainfall from short records: Estimation of high quantiles and impact of measurement errors. *Advances in Water Resources*, 117, 27-39

Marra, F., Zoccatelli, D., Armon, M., Morin, E. (2019). A simplified MEV formulation to model extremes emerging from multiple underlying processes. *Advances in Water Resources*, 127, 280-290

Miao, C., Ashouri, H., Hsu, K., Sorooshian, S., Duan, Q. (2015). Evaluation of the PERSIANN-CDR daily rainfall estimates in capturing the behaviour of extreme precipitation events over China. *Journal of Hydrometeorology*, 16, 1387–1396

Michaelides, S., Levizzani, V., Anagnostou, E.N., Bauer, P., Kasparis, T., Lane, J.E. (2009). Precipitation: measurement, remote sensing, climatology and modeling. *Atmospheric Research*, 94, 512-533

Miniussi, A., Marani, M. (2020). Estimation of daily rainfall extremes through the metastatistical extreme value distribution: Uncertainty minimization and implications for trend detection. *Water Resources Research*, 56, e2019WR026535

Miniussi, A., Marra, F. (2021). Estimation of extreme daily precipitation return levels at-site and in ungauged locations using the simplified MEV approach. *Journal of Hydrology*, 603, 126946

Myhre, G., Alterskjær, K., Stjern, C.W., Hodnebrog, Ø., Marelle, L., Samset, B.H., Sillmann, J., Schaller, N., Fischer, E., Schulz, M., Stohl, A. (2019). Frequency of extreme precipitation increases extensively with event rareness under global warming. *Nature scientific reports* 9, 16063

NASA, IMERG V06: Documentation, https://gpm.nasa.gov/data/imerg

Nerantzaki, S.D, Papalexiou, S.M. (2022). Assessing extremes in hydroclimatology: A review on probabilistic methods. *Journal of Hydrology*, 605, 127302

Papalexiou, S. M. (2018). Unified theory for stochastic modelling of hydroclimatic processes: Preserving marginal distributions, correlation structures, and intermittency. *Advances in Water Resources*, 115, 234-252

Prakash, S., Mitra, A.K., Pai, D.S., AghaKouchak, A. (2015). From TRMM to GPM: how well can heavy rainfall be detected from space? *Advances in Water Resources*, 88, 1-7

Rudolf, B., Schneider, U. (2005). Calculation of gridded precipitation data for the global land-surface using in-situ gauge observations. *Proceedings of the 2nd Workshop of the International Precipitation Working Group IPWG*, 231–247.

Sharon, D. (1972). The spottiness of rainfall in a desert area. *Journal of Hydrology*, 17(3), 161-175

Simpson, J., Kummerow, C., Tao, W.K., Adler, R.F. (1996). On the Tropical Rainfall Measuring Mission (TRMM). *Meteorology and Atmospheric Physics*, 60, 19-36

Tan, j., Huffman G.J., Bolvin D.T., Nelkin, E. (2018). The New IMERG V06: Improvements and Evaluation *AGU Fall Meeting Abstracts*, H41H-20

WegenerNet DataPortal, Stations location info and documentation, https://wegenernet.org/portal/

Weibull, W. (1951). A Statistical Distribution Function of Wide Applicability. *Journal of Applied Mechanics*, 18, 239-296

Wilson, P.S., Tuomi, R., (2005). A fundamental probability distribution for heavy rainfall. *Geophysical Research Letters*, 32, L14812

Zoccatelli, D., Marra, F., Armon, M., Rinat, Y., Smith, J., Morin, E. (2019). Contrasting rainfall-runoff characteristics of floods in desert and Mediterranean basins. *Hydrology and Earth System Sciencies*, 23, 2665–2678

Zorzetto, E., Botter, G., Marani, M. (2016). On the emergence of rainfall extremes from ordinary events. *Geophysical Research Letters*, 43, 8076-8082